Modeling Radionuclide Transport in Clays

Fuel Cycle Research & Development

Prepared for
U.S. Department of Energy
Used Fuel Disposition

Liange Zheng
Lianchong Li
Jonny Rutqvist
Huihai Liu
Jens Birkholzer
Lawrence Berkeley National Laboratory

May, 2012

FCRD-UFD-2012-000128

FCT Quality Assurance Program Document Revision 1 08/19/2011

Appendix E
FCT Document Cover Sheet

Name/Title of Deliverable/Milestone: Modeling of radionuclide transport in clays

Work Package Title and Number: FT-12LB080706
Natural Systems Evaluations - LBNL

Work Package WBS Number: 1.02.08.07

Responsible Work Package Manager: Hui-Hai Liu (Name/Signature)

Date Submitted: 05-21-2012

Quality Rigor Level for Deliverable/Milestone: ☐ QRL-3 ☐ QRL-2 ☐ QRL-1 ☒ N/A* ☐ Nuclear Data

This deliverable was prepared in accordance with: Lawrence Berkeley National Laboratory
(Participant/National Laboratory Name)

QA program which meets the requirements of
☒ DOE Order 414.1 ☐ NQA-1-2000 ☐ Other

This Deliverable was subjected to:

☐ Technical Review ☐ Peer Review

Technical Review (TR)

Review Documentation Provided
- ☐ Signed TR Report or,
- ☐ Signed TR Concurrence Sheet or,
- ☐ Signature of TR Reviewer(s) below

Peer Review (PR)

Review Documentation Provided
- ☐ Signed PR Report or,
- ☐ Signed PR Concurrence Sheet or,
- ☐ Signature of PR Reviewer(s) below

Name and Signature of Reviewers

**NOTE In some cases there may be a milestone where an item is being fabricated, maintenance is being performed on a facility, or a document is being issued through a formal document control process where it specifically calls out a formal review of the document. In these cases, documentation (e.g., inspection report, maintenance request, work planning package documentation or the documented review of the issued document through the document control process) of the completion of the activity along with the Document Cover Sheet is sufficient to demonstrate achieving the milestone. QRL for such milestones may be also be marked N/A in the work package provided the work package clearly specifies the requirement to use the Document Cover Sheet and provide supporting documentation.*

This page is intentionally blank.

CONTENTS

FIGURES

TABLES

ACRONYMS

BBM	Barcelona Basic Model
DDL	Diffuse Double Layer
DRZ	Disturbed Rock Zone
EBS	Engineered Barrier System
EDZ	Excavation Damaged Zone
NBS	Natural Barrier System
THC	Thermal, Hydrological, and Chemical
THM	Thermal, Hydrological and Mechanical
THMC	Thermal, Hydrological, Mechanical, and Chemical
UFD	Used Fuel Disposition

1. INTRODUCTION

Clay/shale has been considered as potential host rock for geological disposal of high-level nuclear waste throughout the world, because of its low permeability, low diffusion coefficient, high retention capacity for radionuclides, and capability to self-seal fractures induced by tunnel excavation. For example, Callovo-Oxfordian argillites at the Bure site, France (Fouche et al., 2004), Toarcian argillites at the Tournemire site, France (Patriarche et al., 2004), Opalinus Clay at the Mont Terri site, Switzerland (Meier et al., 2000), and Boom clay at the Mol site, Belgium (Barnichon and Volckaert, 2003) have all been under intensive scientific investigation (at both field and laboratory scales) for understanding a variety of rock properties and their relationships to flow and transport processes associated with geological disposal of nuclear waste. Clay/shale formations may be generally classified as indurated or plastic clays (Tsang and Hudson, 2010). The latter (including Boom clay) is a softer material without high cohesion; its deformation is dominantly plastic.

During the lifespan of a clay repository, the repository performance is affected by complex thermal, hydrogeological, mechanical, chemical (THMC) processes, such as heat release due to radionuclide decay, multiphase flow, formation of damage zones, radionuclide transport, waste dissolution, and chemical reactions. All these processes are related to each other. An in-depth understanding of these coupled processes is critical for the performance assessment (PA) of the repository. These coupled processes may affect radionuclide transport by changing transport paths (e.g., formation and evolution of excavation damaged zone (EDZ)) and altering flow, mineral, and mechanical properties that are related to radionuclide transport. While radionuclide transport in clay formation has been studied using laboratory tests (e,g, Appelo et al. 2010, Garcia-Gutierrez et al., 2008, Maes et al., 2008), short-term field tests (e.g. Garcia-Gutierrez et al. 2006, Soler et al. 2008, van Loon et al. 2004, Wu et al. 2009) and numerical modeling (de Windt et al. 2003; 2006), the effects of THMC processes on radionuclide transport are not fully investigated.

The objectives of the research activity documented in this report are to improve a modeling capability for coupled THMC processes and to use it to evaluate the THMC impacts on radionuclide transport. This research activity addresses several key Features, Events and Processes (FEPs), including FEP 2.2.08, Hydrologic Processes, FEP 2.2.07, Mechanical Processes and FEP 2.2.09, Chemical Process—Transport, by studying near-field coupled THMC processes in clay/shale repositories and their impacts on radionuclide transport.

This report documents the progress that has been made in FY12. Section 2 discusses the development of THMC modeling capability. Section 3 reports modeling results of THMC impacts on radionuclide transport. Planned work for the remaining months of FY12 and proposed work for FY13 are presented in Section 4.

2. TECHNICAL APPROACHES

This section presents technical approaches used to model THMC processes and their impacts on the migration of U(VI), a common radionuclide.

2.1 Simulator

The numerical simulations are conducted with TOUGHREACT-FLAC3D, which integrates TOUGH-FLAC (Rutqvist et al., 2011) and TOUGHREACT Version 2 (Xu et al., 2011). TOUGH-FLAC3D sequentially couples the finite-difference geomechanical code FLAC3D with the finite-volume, multiphase fluid flow code, TOUGH2 (Pruess et al., 1999).

TOUGHREACT is a numerical simulator for chemically reactive nonisothermal flows of multiphase fluids in porous and fractured media (Xu and Pruess, 2001; Spycher et al., 2003; Sonnenthal et al., 2005; Xu et al., 2006; Xu, 2008; Zhang et al., 2008; Zheng et al., 2009). The code was written in Fortran 77 and developed by introducing reactive chemistry into the multiphase fluid and heat flow simulator TOUGH2 (Pruess, 2004). The code can be applied to one-, two- or three-dimensional porous and fractured media with physical and chemical heterogeneity, and can accommodate any number of chemical species present in liquid, gas, and solid phases. A variety of subsurface thermal, physical, chemical, and biological processes are considered in TOUGHREACT code under a wide range of conditions of pressure, temperature, water saturation, ionic strength, and pH and Eh. TOUGHREACT Version 2 (Xu et al., 2011) is the latest version of TOUGHREACT. The major chemical reactions that can be considered in TOUGHREACT include aqueous complexation, acid-base, redox, gas dissolution/ exsolution, cation exchange mineral dissolution/precipitation, and surface complexation.

TOUGHREACT-FLAC3D was linked in Zheng et al. (2011) to provide the necessary numerical framework for modeling the fully coupled THMC processes. The usefulness of this modeling capability has been demonstrated for modeling of bentonite swelling as a result of changes in saturation and pore-water composition using a simple linear elastic swelling model. In this study, TOUGHREACT-FLAC3D is further enhanced by incorporating a new sorption model for U(VI), to be discussed later.

2.2 An elastic model for chemical-mechanical coupling.

A detailed discussion of TOUGH-FLAC and its capability to simulate THM deformation is presented in Rutqvist et al. (2011). TOUGHREACT-FLAC3D has the same capability for modeling THM processes. In addition, it has the capability to handle coupling between chemical and mechanical processes. While incorporation of more advanced approaches for handing this coupling into TOUGHREACT-FLAC3D is under consideration, this study employs the relatively simple approach of Laredj et al. (2010).

Laredj et al. (2010) extended the nonlinear elastic model for mechanical deformation (Thomas and He, 1995) by adding a chemical concentration term. It is assumed that the increment of total strain is the sum of the strain increments due to the changes in net mean stress, suction, and chemical solute concentration:

$$d\varepsilon = d\varepsilon_p + d\varepsilon_s + d\varepsilon_n \tag{1}$$

where the subscripts p, s, and n refer to net mean stress, suction, and chemical solute concentrations, respectively. The stress-strain relationship can be expressed as:

$$\begin{aligned} d\sigma &= D(d\varepsilon - d\varepsilon_s - d\varepsilon_n) \\ &= D(d\varepsilon - A_s ds - A_n dn) \end{aligned} \tag{2}$$

with

$$d\varepsilon_s = A_s ds \tag{3}$$

$$d\varepsilon_n = A_n dn \tag{4}$$

where D is the elastic matrix, σ is the effective stress and A_s and A_n are constants. Laredj et al. (2010) derived the relation between chemical concentration variation and the corresponding strain and proposed the following expression for A_n:

$$A_n = -\frac{(5.312\ln c - 23.569)}{\sqrt{n}} - \frac{7.252\times10^{-4}}{n^2} \quad (5)$$

Rutqvist et al. (2011) included a linear elastic swelling model using a swelling stress, σ_s, that is linearly proportional to the saturation:

$$d\sigma_s = 3K\beta_{sw}ds_l \quad (6)$$

where K is the bulk modulus and β_{sw} is a moisture swelling coefficient.

To consider the swelling due to both moisture and chemical concentration change, we include the stress due to a chemical concentration change in Equation (7):

$$d\sigma_s = 3K\beta_{sw}ds_l + A_n dn \quad (7)$$

2.3 Chemical Model

As previously indicated, TOUGHREACT-FLAC3D considers a number of chemical reactions that are relevant to radionuclide transport, including aqueous complexation, mineral dissolution/precipitation, cation exchange and surface complexation. In this section, we present the reactions that are directly related to U(VI) only.

2.3.1 Aqueous complexation of U(VI)

Aqueous complexes considered in this study are listed in Table 1. Reaction constants are taken from Spycher et al. (2011); most of them are largely consistent with those used in Davis et al. (2004). Among these aqueous species, the dominant ones are $Ca_2UO_2(CO_3)^3$ and $CaUO_2(CO_3)_3^{-2}$. A chemical-reaction model that neglects these two species could significantly underestimate the aqueous concentration of U(VI).

Table 1. Aqueous complexes for U(VI)

Aqueous complexes	Reactions								Logk (25 °C)
	Stoi.	Species	Stoi.	Species	Stoi.	Species	Stoi.	Species	
$(UO_2)_{11}(CO_3)_6(OH)_{12}^{-2}$	-18	H^+	6	HCO_3^-	11	UO_2^{+2}	12	H_2O	25.855
$(UO_2)_2(OH)_2^{+2}$	-2	H^+	2	H_2O	2	UO_2^{+2}			5.659
$(UO_2)_2CO_3(OH)_3^-$	-4	H^+	1	HCO_3^-	2	UO_2^{+2}	3	H_2O	11.245
$(UO_2)_2OH^{+3}$	-1	H^+	1	H_2O	2	UO_2^{+2}			2.729
$(UO_2)_3(CO_3)_6^{-6}$	-6	H^+	3	UO_2^{+2}	6	HCO_3^-			8.099
$(UO_2)_3(OH)_4^{+2}$	-4	H^+	3	UO_2^{+2}	4	H_2O			11.962
$(UO_2)_3(OH)_5^+$	-5	H^+	3	UO_2^{+2}	5	H_2O			15.624
$(UO_2)_3(OH)_7^-$	-7	H^+	3	UO_2^{+2}	7	H_2O			32.2
$(UO_2)_3O(OH)_2(HCO_3)^+$	-4	H^+	1	HCO_3^-	3	H_2O	3	UO_2^{+2}	9.746
$(UO_2)_4(OH)_7^+$	-7	H^+	4	UO_2^{+2}	7	H_2O			21.995
$UO_2(SO_4)_2^{-2}$	1	UO_2^{+2}	2	SO4--					-3.962
UO_2Cl^+	1	Cl^-	1	UO_2^{+2}					-0.141
$UO_2Cl_2(aq)$	1	UO_2^{+2}	2	Cl^-					1.146
UO_2F^+	1	F^-	1	UO_2^{+2}					-5.034
$UO_2F_2(aq)$	1	UO_2^{+2}	2	F^-					-8.519
$UO_2F_3^-$	1	UO_2^{+2}	3	F^-					-10.762
$UO_2F_4^{-2}$	1	UO_2^{+2}	4	F^-					-11.521
$UO_2OSi(OH)_3^+$	-1	H^+	1	$SiO_2(aq)$	1	UO_2^{+2}	2	H_2O	2.481
$UO_2SO_4(aq)$	1	SO_4^{-2}	1	UO_2^{+2}					-3.049
UO_2OH^+	-1	H^+	1	H_2O	1	UO_2^{+2}			5.218
$UO_2(OH)_2(aq)$	-2	H^+	2	H_2O	1	UO_2^{+2}			12.152
$UO_2(OH)_4^{-2}$	-4	H^+	1	UO_2^{+2}	4	H_2O			32.393
$UO_2CO_3(aq)$	-1	H^+	1	HCO_3^-	1	UO_2^{+2}			0.396
$UO_2(CO_3)_2^{-2}$	-2	H^+	2	HCO_3^-	1	UO_2^{+2}			4.048
$UO_2(CO_3)_3^{-4}$	-3	H^+	3	HCO_3^-	1	UO_2^{+2}			9.141
$CaUO_2(CO_3)_3^{-2}$	-3	H^+	1	Ca^{+2}	3	HCO_3^-	1	UO_2^{+2}	3.806
$Ca_2UO_2(CO_3)_3$	-3	H^+	2	Ca^{+2}	3	HCO_3^-	1	UO_2^{+2}	0.286

2.3.2 Sorption reactions

Adsorption/desorption is another important reaction controlling the migration of U(VI) in clay formations. The adsorption/desorption of uranium onto different types of sediments has been widely studied. Although there are still some reactive transport models utilizing the distribution coefficient (constant-Kd) modeling approach to describe the retardation of uranium in aquifers caused by adsorption reactions (Bethke and Brady, 2000), surface complexation models are currently the most popular ones for calculating the adsorption/desorption of uranium. Typically, surface complexation reactions (including the relevant surface species, the binding constants, and the stoichiometry of the mass action equations) are derived by fitting the macroscopic dependence of adsorption as a function of pH (Davis et al., 1998). Surface reactions can be coupled with aqueous complexation reactions to simulate macroscopic sorption as a function of aqueous chemical conditions.

Although numerous surface complexation models have been developed to describe the sorption of uranium on clay minerals, these models differ in many details and generally lack consistency.

First, models differ in the types of sites. Clay minerals, such as illite, kaolinite and smectite, usually have two types of surface sites: (1) permanent negatively charged sites whose charges are structural (also called basal face sites) and (2) variably charged sites that usually reside at the edge of a mineral (also called edge sites—Gu et al. (2010)). These edge sites were also further divided into aluminol and silanol (McKinley et al. 1995) or even Fe(III)-hydroxyls groups (Tournassat et al. 2004). Also, in studying the sorption of U(IV) on montmorillonite, illite and Opalinus clay formations, Bradbury and Baeyens (2005), Bradbury and Baeyens (2009b), and Bradbury and Baeyens (2011) use two types of sites—one "strong" site and two "weak" sites: the strong sites are analogous to basal face sites, and the weak sites are similar in definition to the edge sites.

Second, these models also differ in the way they account for the electrostatic term— using a triple layer model (McKinley et al. 1995), a double layer model (Arda et al. 2006; Arai et al. 2006), a constant capacity model, or ignoring the electrostatic term (Bradbury and Baeyens 2005; Bradbury and Baeyens 2009b; Bradbury and Baeyens 2011) .

Third, the surface species (i.e., surface complexation binding of U(VI)) used in the models described above are very different. Sometimes the differentiation of surface species are supported by microscopic experimental results (Catalano and Brown Jr., 2005), but more frequently researchers do so only because more than one reaction is needed to fit the measured data (McKinley et al., 1995). Moreover, the aqueous chemical environment in which the sorption tests were conducted also affects the surface species that forms. For example, the model in Korichi and Bensmali (2009) was developed in the absence of Ca^{+2} and the model of Gao et al. (2010) did not consider Ca and CO_3^{-2}.

In this study, we use the so called two-site protolysis nonelectrostatic surface complexation and cation exchange sorption model (2 SPNE SC/CE) (Bradbury and Baeyens, 2011). In this model, surface protonation reactions that involve a strong site (ill_sOH or mon_sOH) and two weak sites (ill_w1OH, ill_w2OH or mon_w1OH, mon_w2OH) are used to describe acid-base titration measurements, whereas surface complexation reactions with the one strong site and two weak sites are needed to describe the sorption edge and isotherm measurements for the sorption of U(VI) on montmorillonite and illite. A detailed discussion of the 2 SPNE SC/CE model for montmorillonite was given in Bradbury and Baeyens (2005); a similar discussion for illite was given in Bradbury and Baeyens (2009a) and Bradbury and Baeyens (2009b). The first twelve reactions listed in Table 2 are the surface protonation reactions on montmorillonite and illite (Bradbury and Baeyens, 2009b), the next six reactions are the surface complexation reactions for the sorption of U(VI) on illite, and the last six reactions are the surface complexation reactions for the sorption of U(VI) on montmorillonite.

Table 2. The surface protonation reactions on montmorillonite and illite and surface complexation reactions for the sorption of U(VI) on montmorillonite and illite (Bradbury and Baeyens, 2009b)

Surface complexation	**logK**
$ill\_sOH_2^+ = ill\_sOH + H^+$	-4
$ill\_sO^- + H^+ = ill\_sOH$	6.2
$ill\_w1OH_2^+ = ill\_w1OH + H^+$	-4
$ill\_w1O^- + H^+ = ill\_w1OH$	6.2
$ill\_w2OH_2^+ = ill\_w2OH + H^+$	-8.5
$ill\_w2O^- + H^+ = ill\_w2OH$	10.5
$mon\_sOH_2^+ = mon\_sOH + H^+$	-4.5
$mon\_sO^- + H^+ = mon\_sOH$	7.9
$mon\_w1OH_2^+ = mon\_w1OH + H^+$	-4.5
$mon\_w1O^- + H^+ = mon\_w1OH$	7.9
$mon\_w2OH_2^+ = mon\_w2OH + H^+$	-6
$mon\_w2O^- + H^+ = mon\_w2OH$	10.5
$ill\_sOUO_2^+ + H^+ = ill\_sOH + UO_2^{+2}$	-2
$ill\_sOUO_2OH + 2H^+ = ill\_sOH + UO_2^{+2} + H_2O$	3.5
$ill\_sOUO_2(OH)_2^- + 3H^+ = ill\_sOH + UO_2^{+2} + 2H_2O$	10.6
$ill\_sOUO_2(OH)_3^{-2} + 4H^+ = ill\_sOH + UO_2^{+2} + 3H_2O$	19
$ill\_w1OUO_2^+ + H^+ = ill\_w1OH + UO_2^{+2}$	-0.1
$ill\_w1OUO_2OH + 2H^+ = ill\_w1OH + UO_2^{+2} + H_2O$	5.3
$mon\_sOUO_2^+ + H^+ = mon\_sOH + UO_2^{+2}$	-3.1
$mon\_sOUO_2OH + 2H^+ = mon\_sOH + UO_2^{+2} + H_2O$	3.4
$mon\_sOUO_2(OH)_2^- + 3H^+ = mon\_sOH + UO_2^{+2} + 2H_2O$	11
$mon\_sOUO_2(OH)_3^{-2} + 4H^+ = mon\_sOH + UO_2^{+2} + 3H_2O$	20.5
$mon\_w1OUO_2^+ + H^+ = mon\_w1OH + UO_2^{+2}$	-0.7
$mon\_w1OUO_2OH + 2H^+ = mon\_w1OH + UO_2^{+2} + H_2O$	5.7

In addition to the surface complexation reactions listed in Table 2, cation exchange reactions are also required to describe the pH sorption edge and isotherm measurement, listed in Table 3.

Table 3. Cation exchange reactions on montmorillonite and illite (Bradbury and Baeyens, 2009b)

Cation exchange reaction	$\mathbf{K_{Na/M}}$
Na^+ + ill-H = ill-Na + H^+	1
Na^+ + ill -K = ill -Na + K^+	0.0775
Na^+ + 0.5 ill -Ca = ill -Na + 0.5Ca^{+2}	0.302
Na^+ + 0.5 ill -Mg = ill -Na + 0.5Mg^{+2}	0.302
Na^+ + 0.5 ill-UO^{+2} = ill-Na + 0.5UO^{+2}	0.473
Na^+ + mon-H = mon -Na + H^+	1
Na^+ + mon -K = mon -Na + K^+	0.0775
Na^+ + 0.5 mon -Ca = mon -Na + 0.5Ca^{+2}	0.302
Na^+ + 0.5 mon -Mg = mon -Na + 0.5Mg^{+2}	0.302
Na^+ + 0.5 mon -UO^{+2} = mon -Na + 0.5UO^{+2}	0.84

2.3.3 Verification of the sorption model with published data

Bradbury and Baeyens (2011) applied the above-mentioned reactions to sorption isotherms of U(VI) on MX-80 bentonite and Opalinus clay. However, some discrepancies were observed between the data and their model results, as illustrated in the following figures. Although they mentioned that a Ca-U-carbonate aqueous complex, i.e., $Ca_2UO_2(CO_3)_3$, was included in their model, it is not clear whether they included other aqueous complexes, which also might have a substantial effect on the data fitting.

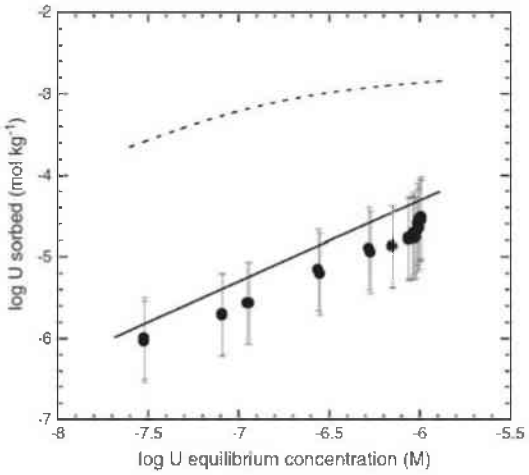

Figure 1. U(VI) sorption isotherm on MX-80 bentonite. Experimental data are shown with marker (●). The dotted line is the blind model prediction without taking into account the formation of the $Ca_2UO_2(CO_3)_3$ aqueous complex. The continuous line is the blind model prediction where the formation of the $UO_2Ca_2(CO_3)_3$ aqueous species was included (Bradbury and Baeyens, 2011).

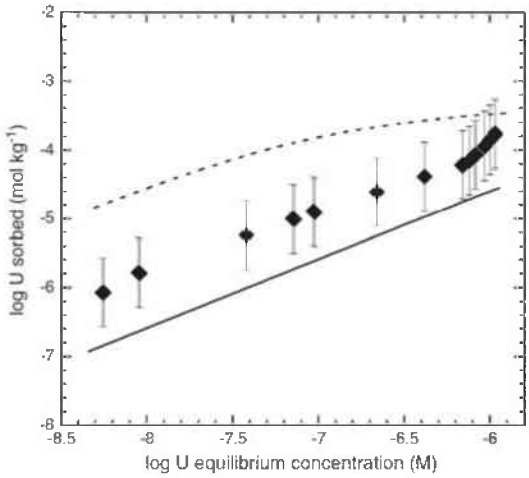

Figure 2. U(VI) sorption isotherm on Opalinus clay. Experimental data are shown with marker (♦). The dotted line is the modeled blind prediction without taking into account the formation of the $UO_2Ca_2(CO_3)_3$ aqueous species. The continuous line is the blind model prediction where the formation of the $Ca_2UO_2(CO_3)_3$ aqueous species was included (Bradbury and Baeyens, 2011).

In order to test our model and improve the match between data and model, reactions in Table 1, 2 and 3 were incorporated into a batch model, and simulations were conducted with TOUGHREACT. The model results are compared with the data reported in Bradbury and Baeyens (2011). MX-80 bentonite contains 75 wt% of montmorillonite (Muller-Vonmoos and Kahr, 1983) and Bradbury and Baeyens (2011) assumed that montmorillonite is the only adsorbent for U(VI). Here, we make the same assumption. Figure 3 shows the calculated U(VI) sorption isotherm for MX-80 bentonite. Model results from TOUGHREACT match closely with the model results of Bradbury and Baeyens (2011).

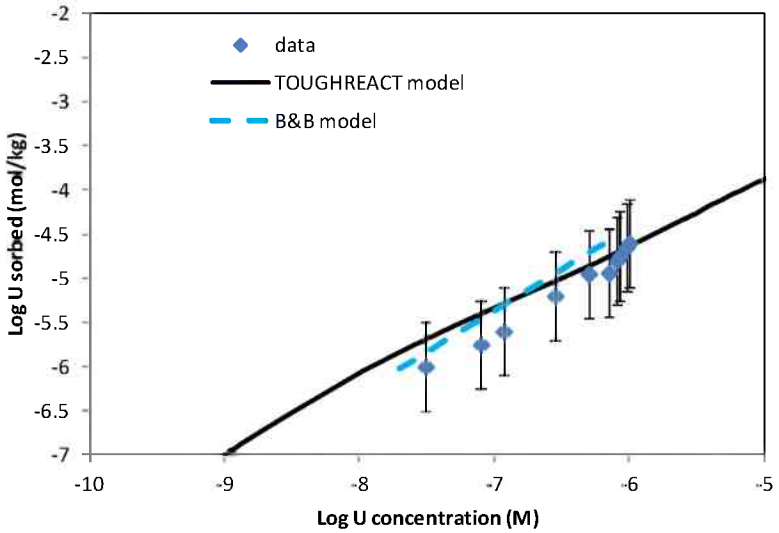

Figure 3. Measured U(VI) sorption isotherm on MX-80 bentonite (Bradbury and Baeyens, 2011) and two models fitting these data. TOUGHREACT model is the model used in this study with all the reactions listed in Tables 1, 2, and 3, while the B&B model shows the model results from Bradbury and Baeyens (2011).

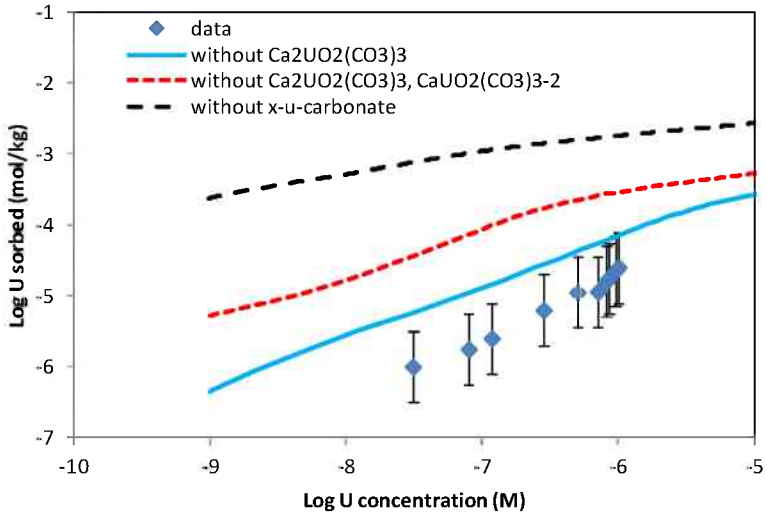

Figure 4. Calculated U(VI) sorption isotherm in three scenarios: without $Ca_2UO_2(CO_3)_3$, without $Ca_2UO_2(CO_3)_3$ and $CaUO_2(CO_3)_3^{-2}$ and without all the aqueous complexes that contain carbonate (where x in " without x-u-carbonate " means Ca and OH and u means UO_2).

As revealed in Bradbury and Baeyens (2011), consideration of a $Ca_2UO_2(CO_3)_3$, makes a significant difference to the sorption isotherm of U(VI). As more aqueous complexes of U(VI) have been reported (e.g., Bernhard et al., 2001; Spycher et al., 2011), they should be included in the geochemical models. For example, in addition to $Ca_2UO_2(CO_3)_3$, $CaUO_2(CO_3)_3^{-2}$ could be another Ca-U-carbonate aqueous complex that could affect the sorption of U(VI). In the TOUGHREACT model shown in Figure 3, all the aqueous complexes listed in Table 1 are included. In order to evaluate how the inclusion of aqueous

complexes affect the calculation of the U(VI) sorption isotherm, we test three scenarios as illustrated in Figure 4: without $Ca_2UO_2(CO_3)_3$, without $Ca_2UO_2(CO_3)_3$ and $CaUO_2(CO_3)_3^{-2}$, and without all the aqueous complexes that contains carbonate. Without including the important aqueous complexes, models tend to overestimate the sorption of U(VI).

Although the amount of illite and illite/smectite mixed layers reported in Lauber et al. (2000) are slightly different from those reported in Thury (2002) (which might be attributed to the different sampling locations), it is clear that Opalinus clay contains around 22% illite and 10–18 wt% of illite/smectite mixed layers. In Bradbury and Baeyens' (2011) model for the sorption of U(VI) on Opalinus clay, they assumed that sorption occured exclusively on illite with mass fraction of 40%. In an effort to reproduce their model within the model "TOUGHREACT model A" in Figure 5, we make the same assumption. Our model deviates from the model of Bradbury and Baeyens (2011) at lower U(VI) concentrations, but matches well at higher U(VI) concentration, This might be caused by the difference in the aqueous complexes and the thermodynamic data. Considering that Opalinus clay also contains some montmorillonite, the model " TOUGHREACT model B" assumes 22% illite and 14% montmorillonite (see Table 5), which, as shown in Figure 5, fits better to the measured U(VI) sorption isotherm.

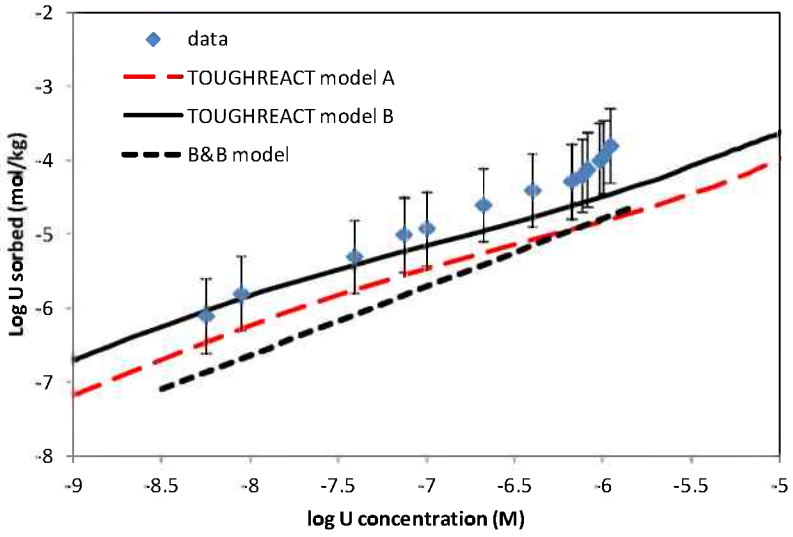

Figure 5. Measured U(VI) sorption isotherm for Opalinus clay (Bradbury and Baeyens, 2011) and three models fitting these data. TOUGHREACT model A and B are models used in this report, with all the reactions listed in Tables 1, 2, and 3; while the B&B model shows the model results from Bradbury and Baeyens (2011).

2.3.4 Uranium minerals

In the geological repository environment, radionuclides originate from used-fuel waste packages. The degradation of these waste packages is an extremely complex issue. Used fuel pellets are largely composed of solid UO_2. Usually, UO_2 would undergo oxidative dissolution with oxidants (typically H_2O_2) produced by α-radiolysis (De Windt et al., 2006): $UO_2(s) + H_2O_2 = UO_2^{+2} + 2OH^-$, U(VI) ($UO_2^{+2}$) is produced and would precipitate as a secondary U(VI) phase. For example, in a 10-year degradation of $UO_2(s)$ by dripping water (Bernot, 2005), 11 phases were identified, including schoepite, soddyite, boltwoodite or na-boltwoodite, and uranophane. The formation of these phases depends on possible

environmental conditions, such as the aqueous and mineralogical composition of the media in contact with the waste package, as well as the pH, Eh, and CO_2 partial pressure. The oxidation of UO_2(s) and the formation of secondary U(VI) phases are slow and usually simulated as kinetics processes (De Windt et al., 2003). However, as the waste packages degrade, the U concentration is controlled by the least soluble uranium phase that is stable under the given geochemical conditions. To be conservative, and for reasons of simplicity, the source concentration of uranium is usually determined by the solubility of the U(VI) phase that is possibly present in the given performance assessment environment. After an evaluation of the possible U(VI) minerals, Bernot (2005) selected schoepite as the controlling phase, because laboratory studies of Wronkiewicz et al. (1996) showed it to be the dominant early-formed phase in UO_2(s) degradation. In this report, we take the same strategy and assume that the waste package is composed only of schoepite; the concentration of U(VI) is then controlled by the following reaction:

$$\text{Schoepite} + 2H^+ = 3H_2O + UO_2^{+2} \quad \log K(25\ ^\circ C) = 4.844 \tag{8}$$

The logK value of the reaction is taken from the EQ3/6 database data0.ymp.R5, and the variation in logK as a function of temperature is given as:

$$\text{LogK}(T) = 14.6\ln(T) - 92.016 - 1.644\times10^{-2}T + 5.5357\times10^{-3}/T \tag{9}$$

where T is temperature (K).

2.4 Model Setup

2.4.1 Model domain

The THMC simulations were conducted for a hypothetical bentonite-back-filled nuclear waste repository in clay rock. The repository example is taken from the DECOVALEX IV project involving a horizontal nuclear waste emplacement tunnel at 500 m depth (Figure 6) (Rutqvist et al., 2009). The problem has been simulated by a number of teams in the DECOVALEX project using simplified models of bentonite behavior.

In this study, a calculation using the improved TOUGHREACT-FLAC3D was carried out with an elastic approach for mechanical deformation, assuming that the rock matrix is isotropic. We constructed a numerical model with a geometry containing one circular tunnel and consisting of 368 grid blocks. The configuration of the model is shown in Figure 7. The Z-axis is set as vertical in the model, while the horizontal Y- and X-axes are aligned parallel and perpendicular to the emplacement tunnel, respectively.

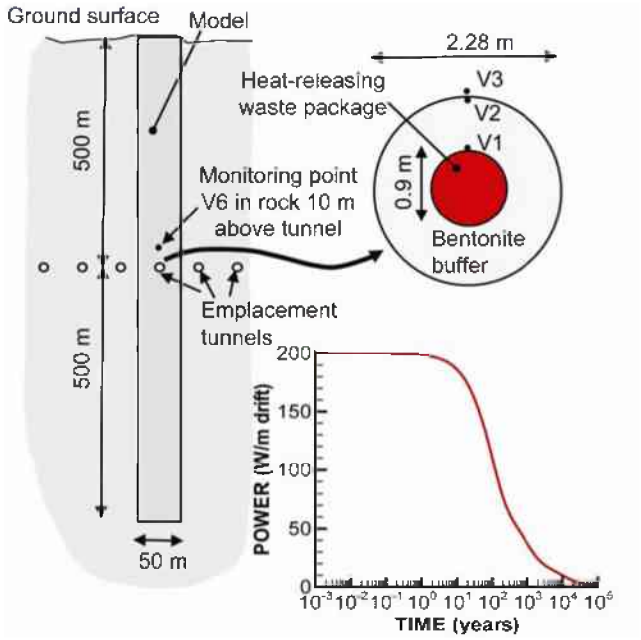

Figure 6. Domain for the test example of a bentonite back-filled horizontal emplacement drift at 500 m (Rutqvist et al., 2009).

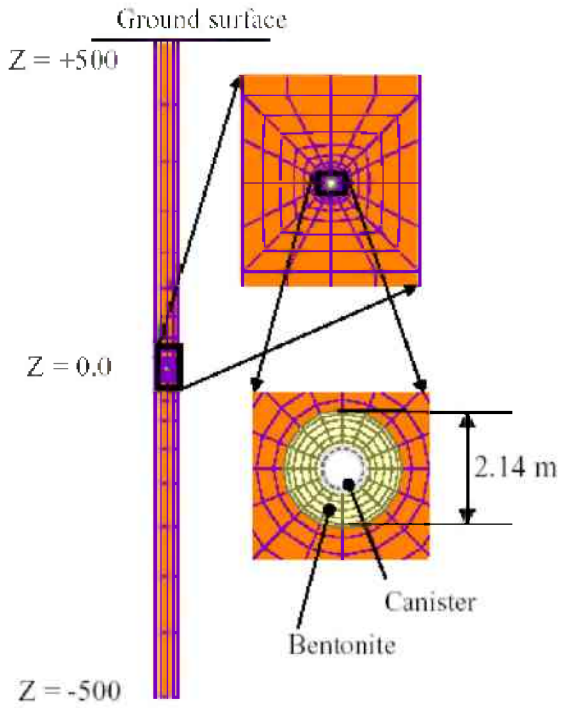

Figure 7. Mesh for modeling of horizontal emplacement drift at 500 m depth.

2.4.2 Initial and boundary conditions

2.4.2.1 THM model

The emplacement tunnel is located at 500 m depth underground, with an initial stress field subjected to the self-weight of the rock mass. Zero normal displacements are prescribed on the lateral boundaries of the model. Vertical displacements are prevented at the bottom. The model simulation was conducted in a non-isothermal mode with a time-dependent heat power input (Rutqvist et al., 2009), adopted from the heat load developed for the Generic Disposal System Environment (GDSE) within the UFD for Pressurized Water Reactor (PWR) used nuclear fuel.

2.4.2.2 Chemical model

In this hypothetical case, it is assumed that the EBS is composed of Kunigel-V1 bentonite (Ochs et al., 2004) and the mineral composition of the bentonite is listed in Table 1. It is also assumed that the host rock is Opalinus clay (Thury, 2002) with the mineral composition listed in Table 2.

Table 4. Mineral composition of the bentonite used in the model (taken from the Kunigel-V1 bentonite (Ochs et al., 2004)).

Mineral	Abundance (volume fraction)
Schoepite	0
Calcite	0.023
Illite	0
Kaolinite	0
chlorite	0
montmorillonite-na	0.475
Quartz	0.335
K-Feldspar	0.041
Siderite	0
Dolomite	0.029
Ankerite	0

Table 5. Mineral composition of the clay formation used in the model (taken from the Opalinus clay (Thury, 2002).

Mineral	Abundance (volume fraction)
Schoepite	0
Calcite	0.1
Illite	0.223
Kaolinite	0.174
Chlorite	0.1445
montmorillonite -na	0.1426
Quartz	0.1845
K-Feldspar	0
Siderite	0.01256
Dolomite	0
Ankerite	0.00798

The pore-water composition of the bentonite (Ochs et al., 2004) and clay formation (Fernandez et al., 2007) are listed in Table 3. Fernandez et al. (2007) conducted five onsite water sampling campaigns from the borehole BDI-B1 (see Table 3). Here, we use the average concentrations of these five campaigns. Note that laboratory-measured pH is used in order to be consistent with concentrations of other chemical species. Although redox potential (Eh) was measured in the field, because it is known (e.g., Appelo and Postma, 1994) that field-measured Eh is hardly reliable, we take the Eh calculated from the redox couple Fe^{+2}/F^{+3} which is 268 mV. Given that the pore water is under mild oxidizing conditions, uranium is likely present in its U(VI) form (UO_2^{+2}).

The initial water for EBS bentonite was taken from Sonnenthal et al. (2008) and used in the benchmark for the DECOVALEX-THMC project (Sonnenthal et al., 2008). For F^-, Br^-, and O_2(aq), which were not reported in Sonnenthal et al. (2008), we simply assumed that they have the same concentration as that in Opalinus clay. F^- and Br^-, though are not of great interest in current simulations, are included to account for their aqueous complexing with U(VI). In TOUGHREACT, redox potential is represented by O_2(aq) concentration.

Table 6. Chemical characteristics of the water samples collected in the different water sampling campaigns from borehole BDI-B1 (Fernandez et al., 2007)

Date	Unit	22/04/2003	25/06/2003	28/10/2003	12/07/2004	01/03/2005	average
EC	(mS/cm)	29.8	26.8	28.1	24.3	26.2	27.04
pH	field	–	6.8	6.9	7	7.6	7.075
pH	lab	7.3	7.5	7.4	7.6	7.6	7.48
Eh	(mV)	n.d.	83	77	-7	-24.2	32.2
Eh	calc.(mV)	316	339	339	228	118	268
F	(mg/L)	0.3	0.3	0.3	0.19	0.51	0.32
I	(mg/L)	2.2	2.2	1.8	2	2.6	2.16
NHþ4	(mg/L)	14.2	12.7	14	13	13	13.38
Br	(mg/L)	31	28	28	19	22	25.6
Cl	(mg/L)	11000	12000	11000	13000	11800	11760
SO4	(mg/L)	2100	1833	1700	1700	1600	1786.6
Alk.cHCO	(mg/L)	344	347	313	303	280	317.4
Fe total	(mg/L)	2.2	4.3	4.1	3.3	1.31	3.042
Fe(II)	(mg/L)	1.3	1.6	1	3.1	1.26	1.652
SiO2	(mg/L)	7.4	9.2	4.2	5.8	8.3	6.98
K	(mg/L)	88	89	93	73	80	84.6
Al	(mg/L)	0.1	0.1	0.1	0.12	<0.05	0.105
Li	(mg/L)	0.8	0.8	n.d.	n.d.	n.d.	0.8
B	(mg/L)	0.1	3.5	3.1	3	2.5	2.44
Ca	(mg/L)	922	1033	886	880	806	905.4
Mg	(mg/L)	611	574	456	505	395	508.2
Na	(mg/L)	6480	6300	6650	6300	6000	6346
Sr	(mg/L)	43	40	41	36	37	39.4
Mn	(mg/L)	0.4	0.3	0.3	0.22	0.12	0.268
Ni	(mg/L)	0.1	<0.03	0.07	<0.03	0.07	0.08
Zn	(mg/L)	33	2.3	0.05	<0.05	<0.05	11.78

Table 7. Pore-water composition of EBS bentonite and host clay rock.

	EBS Bentonite: Kunigel-V1 (Sonnenthal et al., 2008)	**Opalinus Clay (Fernandez et al., 2007)**
pH	8.40	7.40
Eh	0.268	0.268
Cl	1.50E-05	3.32E-01
SO_4^{-2}	1.10E-04	1.86E-02
HCO_3^-	3.49E-03	5.18E-03
Ca^{+2}	1.37E-04	2.26E-02
Mg^{+2}	1.77E-05	2.09E-02
Na^+	3.60E-03	2.76E-01
K^+	6.14E-05	2.16E-03
Fe^{+2}	2.06E-08	3.46E-06
$SiO_2(aq)$	3.38E-04	1.10E-04
AlO_2^-	1.91E-09	3.89E-08
F-	1.68E-05	1.68E-05
Br-	3.2E-04	3.2E-04
$O_2(aq)$	1.07E-41	1.07E-41
UO_2^{+2}	1E-10	1E-10

Table 6 lists the thermal and hydrodynamic parameters used in the model. Those for bentonite are taken from Sonnenthal (2008), while those for clay formations are mostly taken from Thury (2002).

Table 8. Thermal and hydrodynamic parameters.

Parameter	**Clay formation**	**Bentonite**
Grain density [kg/m^3]	2700	2700
Porosity ϕ	0.15	0.41
Saturated permeability [m^2]	5.0×10^{-20}	2.0×10^{-21}
Relative permeability, k_{rl}	$m = 0.6$, $S_{rl} = 0.01$	$K_{rl} = S^3$
Van Genuchten α [1/Pa]	6.8×10^{-7}	3.3×10^{-8}
Van Genuchten m	0.6	0.3
Compressibility, β [1/Pa]	3.2×10^{-9}	5.0×10-8
Thermal expansion coeff., [1/°C]	0.0	1.0×10^{-4}
Dry specific heat, [J/kg °C]	800	8000
Thermal conductivity [W/m °C] dry/wet	2.2/2.2	0.5/1.3
Tortuosity for vapor phase	$\phi^{1/3} S_g^{10/3}$	$\phi^{1/3} S_g^{10/3}$

Mineral dissolution/precipitation is kinetically controlled, except that schoepite is assumed in equilibrium. The kinetic law for mineral dissolution/precipitation is given in Xu et al. (2006). The kinetic rate for the mineral considered in current model is given in Table 7. Note that the surface areas listed in Table 7 are calculated for tuff (Sonnenthal et al., 2005). Their applicability to the clay formation considered is questionable. Further refinement of the surface-area calculation is needed in the future when the THMC model is applied to a realistic scenario.

Table 9. Kinetic properties for minerals considered in the model (Xu et al., 2006)

Mineral	A (cm^2/g)	Parameters for Kinetic Rate Law							
		Neutral Mechanism		Acid Mechanism			Base Mechanism		
		k_{25} ($mol/m^2/s$)	E_a (KJ /mol)	k_{25}	E_a	$n(H^+)$	k_{25}	E_a	$n(H^+)$
Primary:									
Schoepite	Assumed at equilibrium								
Quartz	9.8	1.023×10^{-14}	87.7						
K-feldspar	9.8	3.89×10^{-13}	38	8.71×10^{-11}	51.7	0.5	6.31×10^{-12}	94.1	-0.823
Kaolinite	151.6	6.91×10^{-14}	22.2	4.89×10^{-12}	65.9	0.777	8.91×10^{-18}	17.9	-0.472
Illite	151.6	1.66×10^{-13}	35	1.05×10^{-11}	23.6	0.34	3.02×10^{-17}	58.9	-0.4
Chlorite	9.8	3.02×10^{-13}	88	7.76×10^{-12}	88	0.5			
Calcite	3.5	1.6×10^{-7}	23.5						
Dolomite	12.9	2.52×10^{-12}	62.76	2.34×10^{-7}	43.54	1			
Ankerite	9.8	1.26×10^{-9}	62.76	6.46×10^{-4}	36.1	0.5			
Smectite-Na	151.6	1.66×10^{-13}	35	1.05×10^{-11}	23.6	0.34	3.02×10^{-17}	58.9	-0.4
Na-montmorillonite	151.6	1.66×10^{-13}	35	1.05×10^{-11}	23.6	0.34	3.02×10^{-17}	58.9	-0.4

3. MODELING RESULTS

The model considers a canister, an EBS bentonite and a host clay formation. Initially, the EBS bentonite is under an unsaturated condition, and temperature is 25°C everywhere. The model was run for 10,000 years. It is assumed that canister is broken and U(VI) is released by the dissolution of schoepite after 1000 years. Note that assuming that canister failure would occur in 1000 years is very conservative in comparison with other THC simulations on radionuclide migration. For example, De Windt et al. (2006) assumed that canister failure occurs after 10,000 years. However, after 1000 years, the EBS becomes fully saturated and water-rock interactions are close to equilibrium conditions, THMC processes evolve very slowly thereafter, unless there were some incidents such as earthquakes. In other words, the THMC environment in which radionuclides migrate would not change substantially from 1000 years to 10,000 years. Therefore, it is expected that the starting time of U(VI) release, whether it be 1000 years or 10,000 years, would not affect U(VI) migration significantly.

3.1 THM evolutions

To investigate the THM behavior around the emplacement tunnel, we first present the response induced by heating and hydration processes, based on elastic analysis. THM behavior is described by the temperature, pore pressure, and saturation variations around the repository, as well as the stress distribution at monitoring points A, B, C, and D as marked in Figure 8.

Two simulations are presented here that differ in the elastic model: the first one adopted a linear elastic swelling model as in Equation (6), called THMC1 here; the second one used an elastic swelling model that accounts for both moisture and chemical concentration change as illustrated by Equation (7), called THMC2 here. A comparison of the calculated stress fields from THCM1 and -2 allows us to evaluate the contribution of chemically induced swelling.

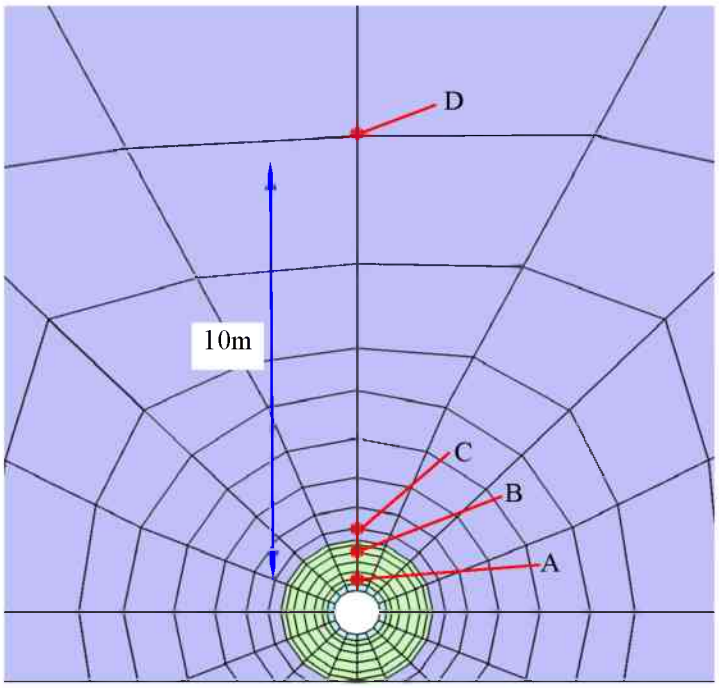

Figure 8. Location of key points for monitoring parameter variations in numerical simulations.

Figure 9 shows the temperature evolution at locations A, B, C, and D; and Figure 10 shows the temperature field at three different elapsed times (at 10, 100, and 10,000 years). It is shown that a maximum temperature of about 90°C is reached at the surface of the waste canister after about 20–30 years. Then, the temperature begins to decline steadily. At 10,000 years, the temperature has declined to about 40°C, which is higher than its initial value. The temperature fields from THMC1 and -2 show no difference, since these two models differ only in chemical-mechanical coupling.

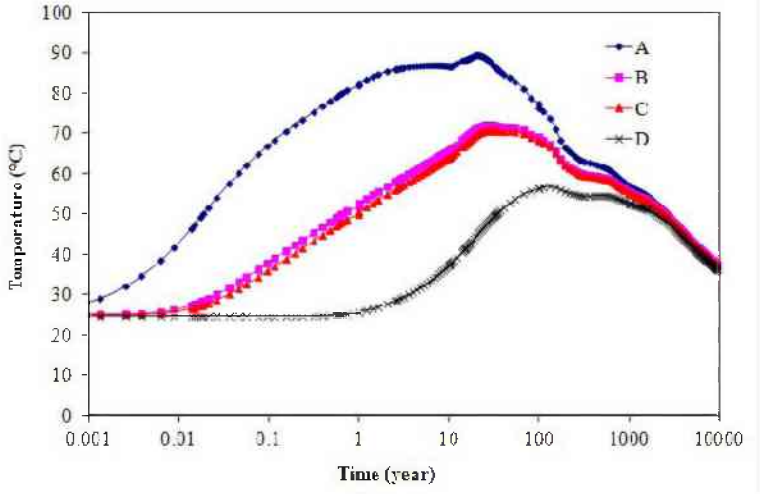

Figure 9. Temperature evolution at points A, B, C, and D.

Figure 11 shows the pore-pressure evolutions at A, B, C, and D; and the contours of the pore pressure at 10, 100, and 10,000 years are displayed in Figure 12. At 10 years, there is an evident increase in pore pressure. A maximum pore pressure of about 3.0 MPa is reached in the host clay formation adjacent to the EBS bentonite after about 100 years. Then, the pore-pressure evolution shows a tendency to stabilize at a constant value from 100 to 2000 years. After 2000 years, the pore pressure begins to decline steadily.

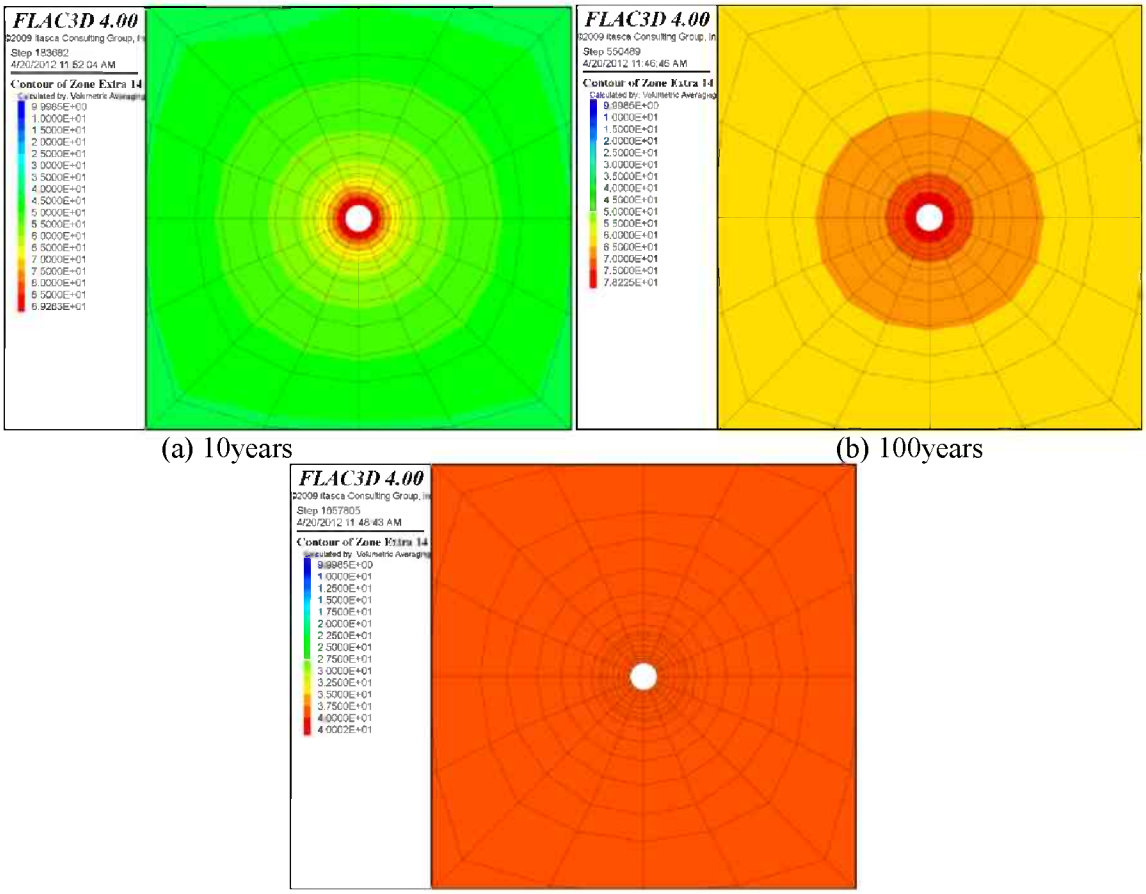

(a) 10years (b) 100years

(c) 10,000years

Figure 10. Temperature evolution around the emplacement tunnel.

Again THMC1 and -2 show no difference in pore-pressure evolution, since these two models differ only in chemical-mechanical coupling.

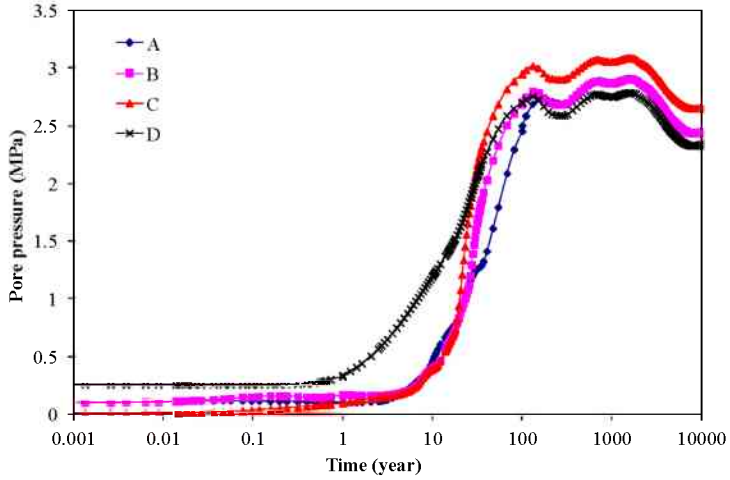

Figure 11. Pore-pressure evolution at points A, B, C, and D.

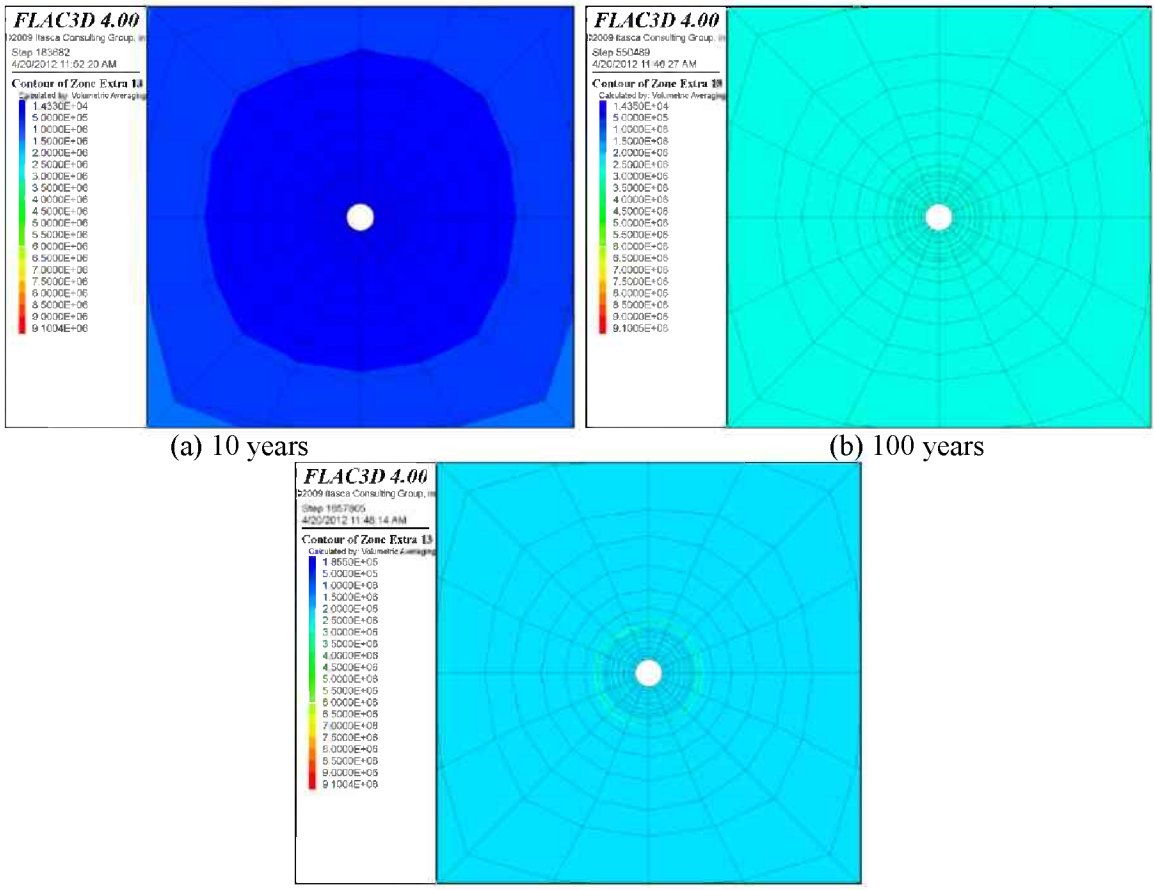

(a) 10 years (b) 100 years

(c) 10,000 years

Figure 12. Pore-pressure evolution around the emplacement tunnel.

Figure 13 shows the saturation evolution at A, B, C, and D; and the contours of the liquid saturation at 10, 100, and 10,000 years are displayed in Figure 14. In the area close to the heater (point A in Figure 13), EBS bentonite undergoes a de-saturation in the first two years caused by the heating from the canister, and then gradually become fully saturated after 20 years. The near-field clay formation in the vicinity of the buffer (point C in Figure 13) desaturates initially because of the relative low permeability of the clay formation. The clay formation is very close to full saturation after 30 years, with a saturation degree larger than 99%, lasting for 10,000 years (Figure 14).

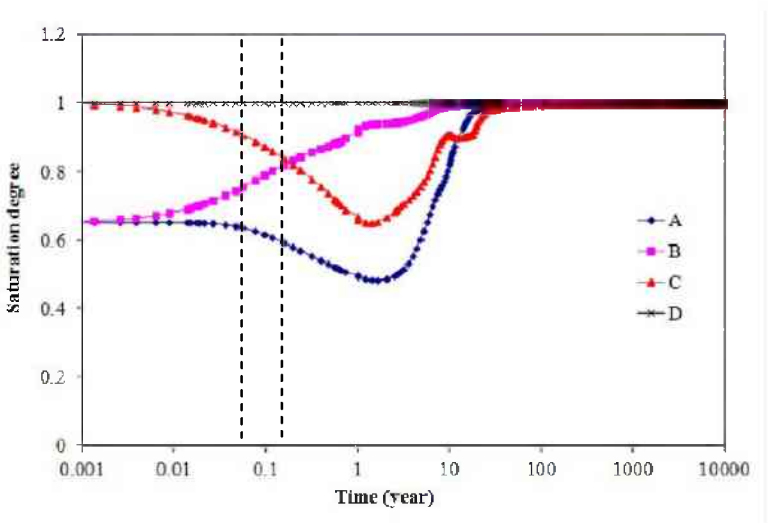

Figure 13. Saturation evolution at points A, B, C, and D.

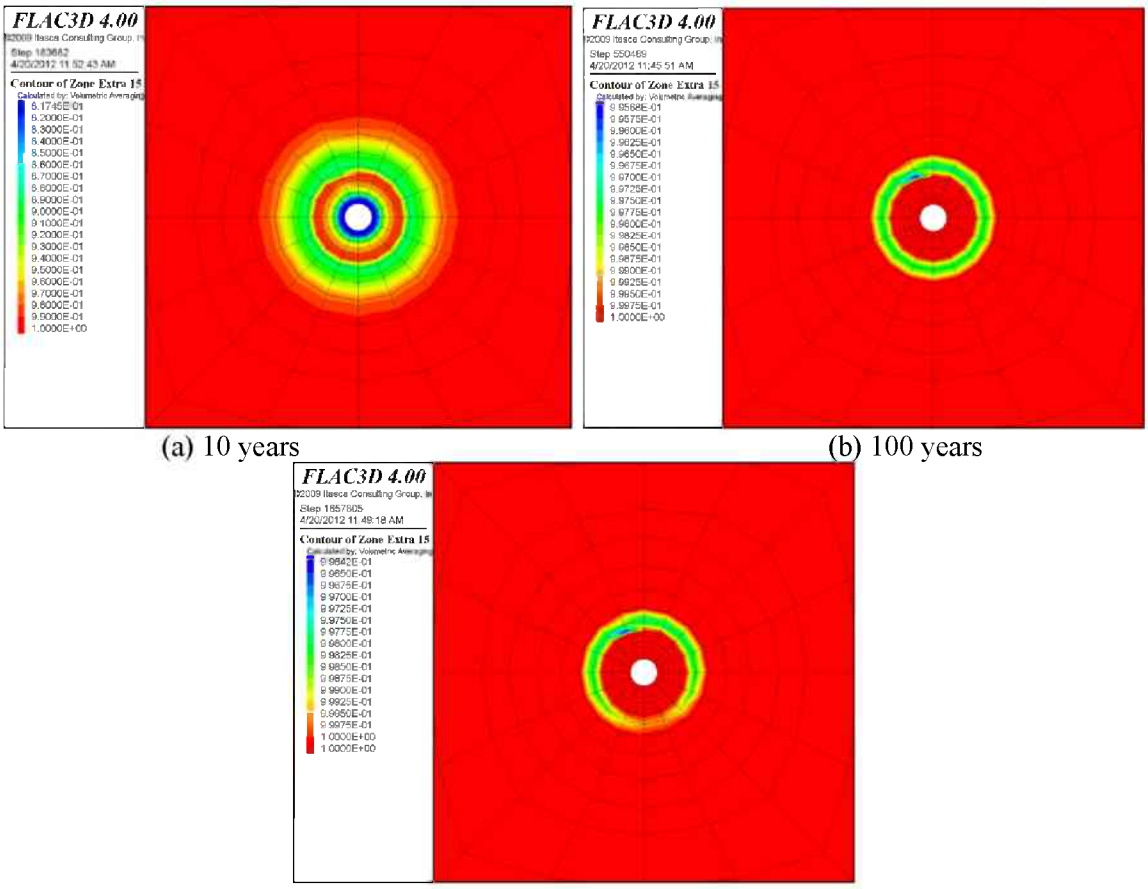

(a) 10 years (b) 100 years

(c) 10,000 years

Figure 14. Saturation evolution around the emplacement tunnel.

The evolution of maximum and minimum compressive principal stresses is the most important factor in determining the state of failure for the rock mass surrounding the deposition hole. Figures 15–19 present the numerical results of THMC1 and -2 for the evolution of stress at points A, B, C, and D as part of the

evaluation of repository stability. Generally, the compressive stress increases with heating before 100 years. At about 10 years, there is an increment of stress, particularly at points A and B. The maximum compressive principal effective stress, $\sigma_1^{'}$, about 9 MPa, is reached at point C (i.e., the location in the rock mass adjacent to the EBS bentonite). The maximum $\sigma_1^{'}$ of about 108 MPa is reached at point C after about 100 years, while the minimum compressive principal effective stress, $\sigma_3^{'}$, is relatively small. The risk for rock failure is the highest at about 100 years. It can thus be concluded that the first 100 years is a key phase for the safety of the repository, when the heat-induced stress plays an important role in the stability of the rock mass surrounding the emplacement tunnel.

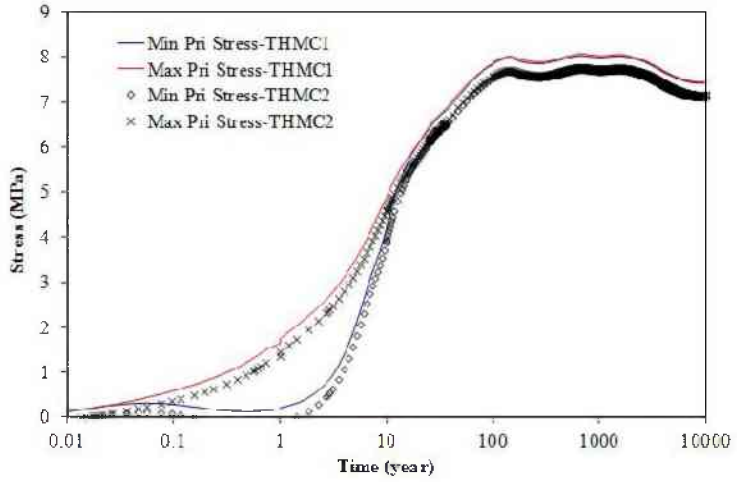

Figure 15. Simulation results of maximum and minimum principal compressive effective stresses ($\sigma_1^{'}$ and $\sigma_3^{'}$) at point A.

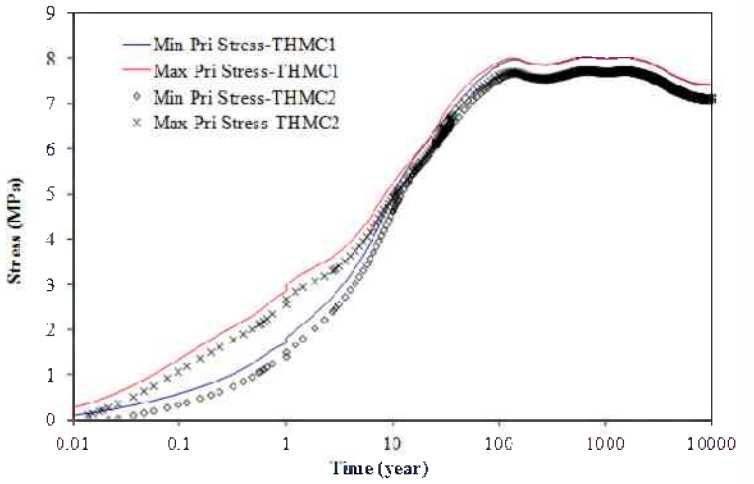

Figure 16. Simulation results of maximum and minimum principal compressive effective stresses ($\sigma_1^{'}$ and $\sigma_3^{'}$) at point B.

Comparisons between the numerical results of THMC1 and -2 show that the stresses (both maximum principal stress and minimum principal stress) within the EBS bentonite are higher in THMC1. The chemically induced swelling accounts for about 5% of the total effective stress. However, the stresses in

the surrounding clay rock (presented by point C and D in Figure 17 and 18) are not evidently different, because the total solute concentration changes within these zones are rather minimal, as shown in the next section.

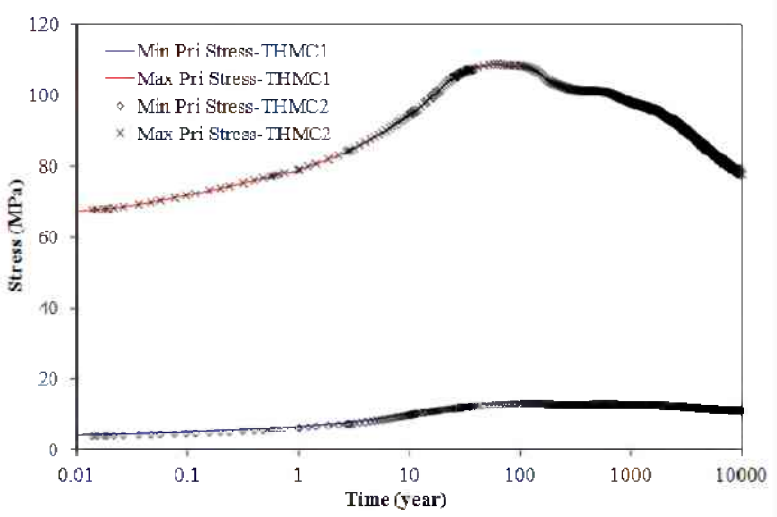

Figure 17. Simulation results of maximum and minimum principal compressive effective stresses ($\sigma_1^{'}$ and $\sigma_3^{'}$) at point C.

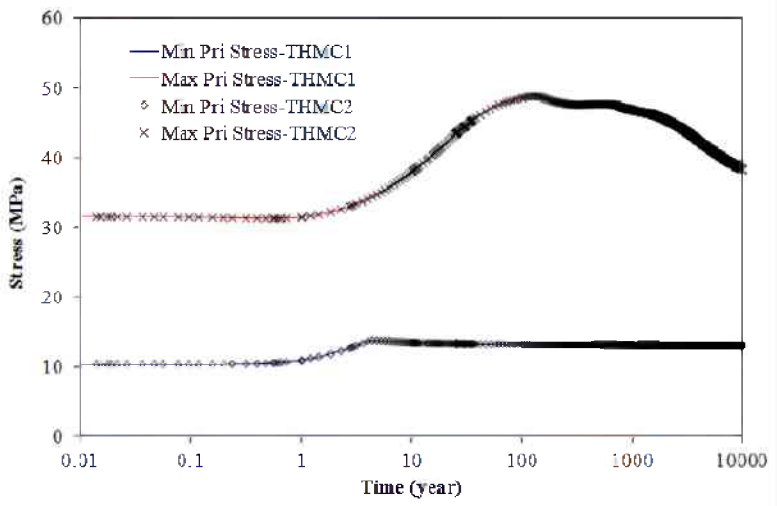

Figure 18. Simulation results of maximum and minimum principal compressive effective stresses ($\sigma_1^{'}$ and $\sigma_3^{'}$) at point D.

3.2 Reactive Transport Simulation Results

3.2.1 Chemical evolution

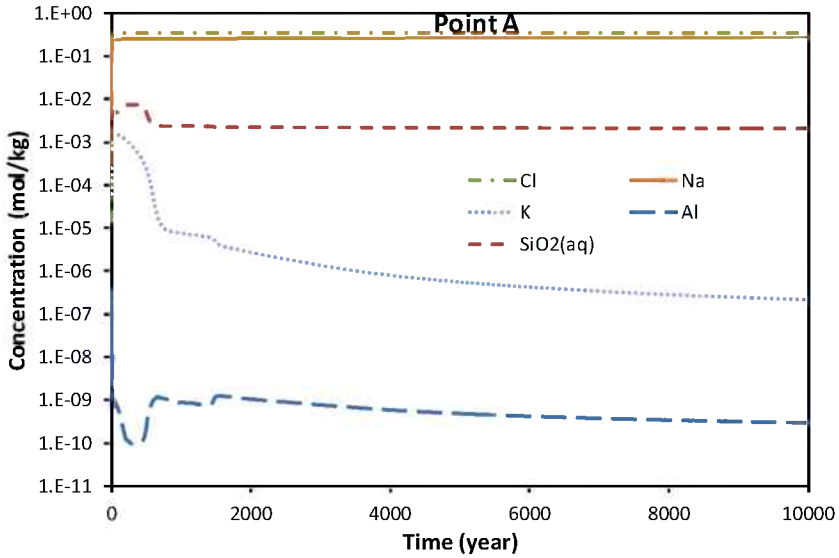

(a)

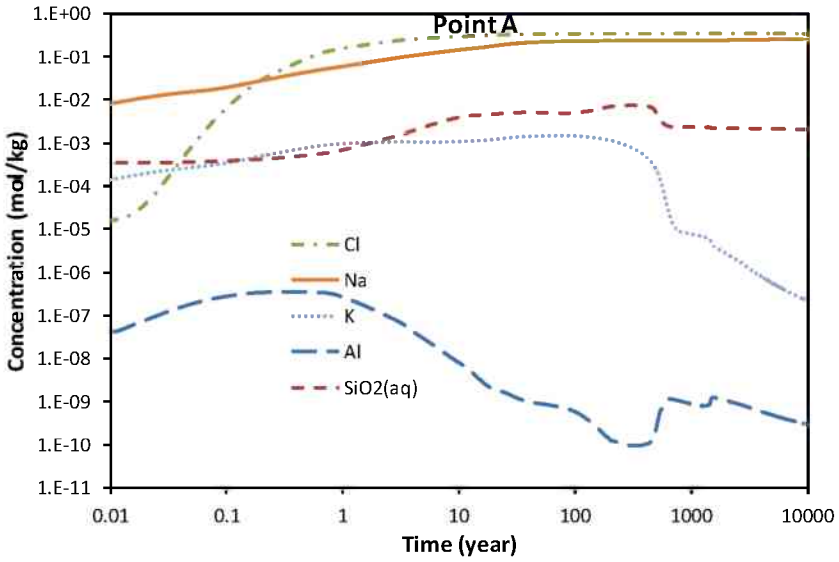

(b)

Figure 19. Time evolution of Cl, Na, and K, Al and SiO_2(aq) concentrations at point A with linear (a) and logarithmic (b) time scale.

Initially, the pore water in EBS bentonite has low concentrations of most species, because diluted water was used to fabricate the bentonite blocks. Chemical reactions could be triggered by several processes, including dispersion (molecular diffusion and hydrodynamic dispersion), mixing caused by the influent of host-clay-formation water, heating from the canister, or the self-adjustment of water composition towards a water-rock equilibrium (given that initial water is usually not under equilibrium with the minerals in the bentonite). The evolution of Cl (Figure 19 a and b) mainly reflects dispersion and mixing. A quick rise in Cl concentration (Figure 19b) indicates that such processes are fairly fast. One reason could be an overestimated dispersion effect. THMC simulations are computationally expensive. Thus, in order to

minimize the number of grid blocks in the model, a relative course mesh is used for EBS. An EBS with a radial distance of about 0.8 m is discretized to six ring layers, which leads to a gridding distance of 0.15 m and a numerical dispersion coefficient of 0.075 m. Such a high dispersion coefficient results in the fast equilibrium of EBS pore water with host clay formation water. Na, while experiencing cation exchange and mineral precipitation/dissolution, seems also largely controlled by mixing between the bentonite pore water and clay-formation water, and dispersion processes; its evolution is similar to that of Cl (Figure 19 a, b).

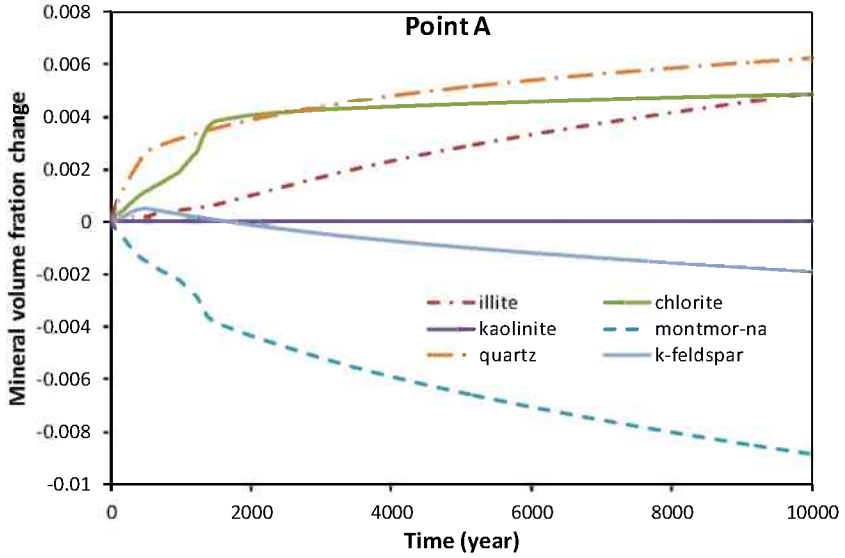

(a)

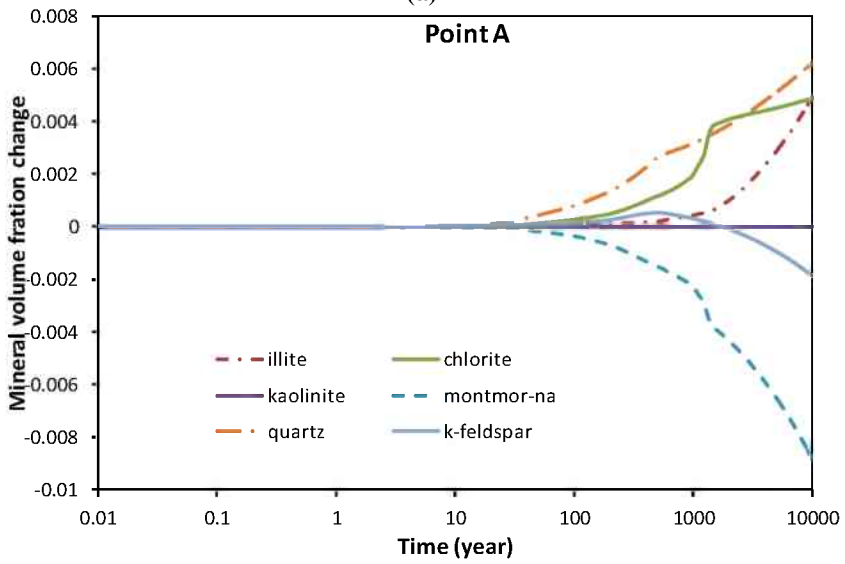

(b)

Figure 20. Time evolution of Si-Al minerals at point A with linear (a) and logarithmic (b) time scale.

K, Al and SiO_2(aq) are chemical species whose evolutions are typically controlled by Si-Al minerals. The diluteness of the initial bentonite pore water suggests that the water composition listed in Table 2 is probably just the recipe of the water that was used to make the bentonite block. Unsurprisingly, bentonite pore water undergoes a quick adjustment of Al and SiO_2(aq) as is determined by the interaction of montmorillonite, illite, chlorite, quartz and k-feldspar. After that, montmorillonite keeps dissolving (Figure 20), which raises the concentration of Al and SiO_2(aq). However, the precipitation of chlorite and

K-feldspar overcome this increase, and consequently the Al concentration keeps dropping, with the lowest point coincidental with the maximum precipitation of K-feldspar at 200–400 years. Afterwards, the K-feldspar starts to dissolve (Figure 20), which leads to a rebounding of Al concentration (Figure 19) to a relatively steady level after 600 years. This steady level is maintained as the dissolution of montmorillonite and the precipitation of chlorite and illite is maintained at a relatively constant rate, until 1400 to 1500 years. After that, the Al concentration increases slightly because chlorite precipitation slows down due to the limited availability of Fe.

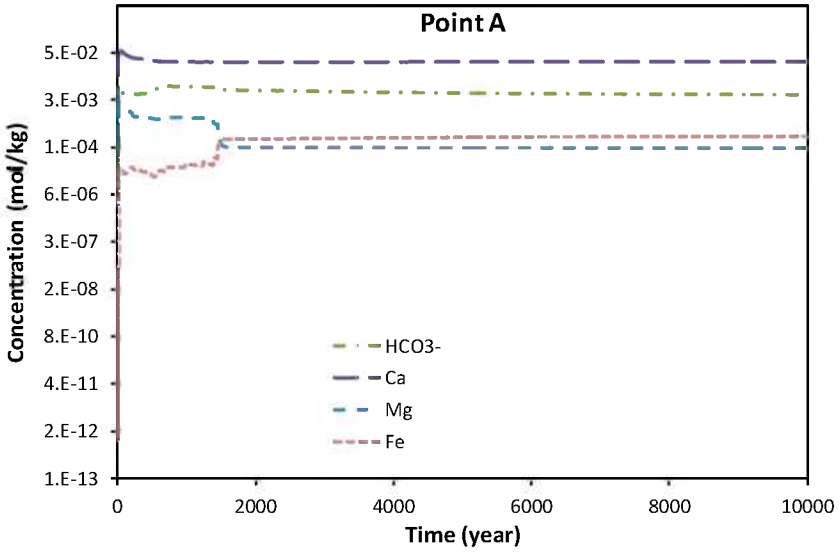

(a)

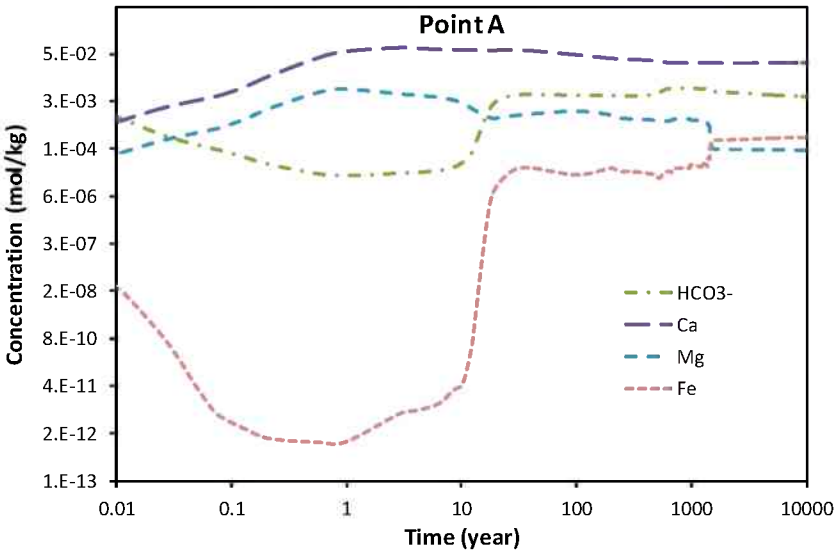

(b)

Figure 21. Time evolution of Ca, Mg, Fe, and HCO_3^- concentrations at point A with linear (a) and logarithmic (b) time scale.

Potassium (K) concentrations undergo a rapid increase (Figure 19), caused by the influent of clay-formation water that contains higher K concentration (see Table 2). This increase induces the precipitation of illite and K-feldspar, and consequently the concentration of K drops quickly until 600 years, when the precipitation of K-feldspar stops. After that, the K concentration keeps dropping at a

relatively slow pace, corresponding to the precipitation of illite, until 1400 to 1500 years. At that time, the precipitation of chlorite slows down significantly and more Al is available for the illite precipitation, so that illite precipitation increases and causes a further sharp drop K concentration. Later on, illitization processes, i.e., the transformation of montmorillonite to illite, continues, and K concentration decreases at a slow, steady pace.

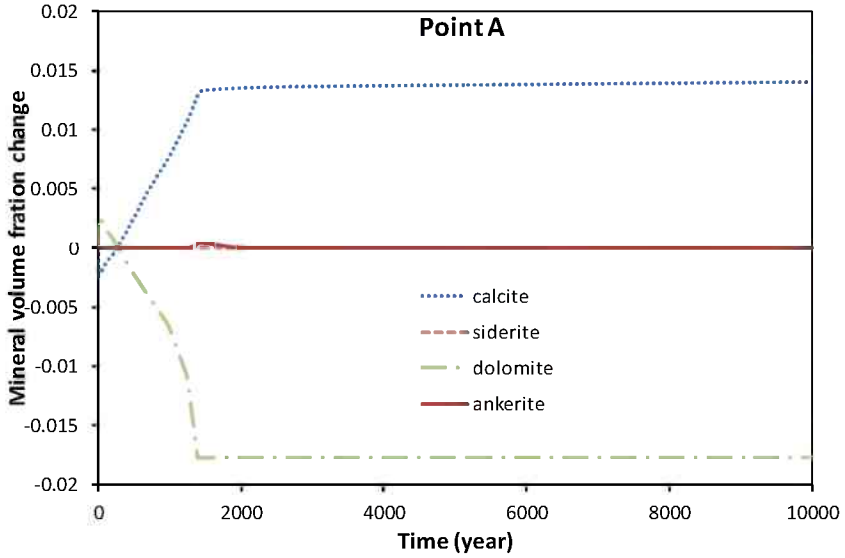

(a)

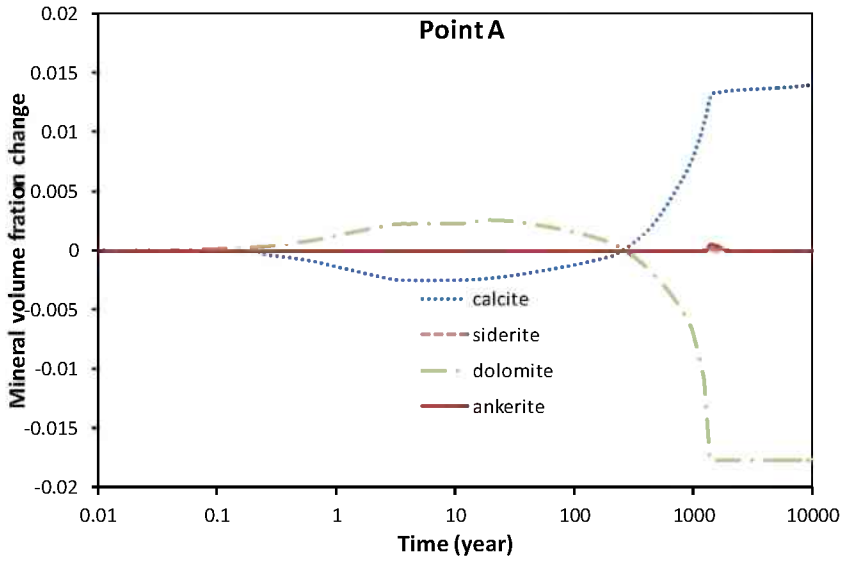

(b)

Figure 22. Time evolution of carbonate minerals at point A with linear (a) and logarithmic (b) time scale.

The initial concentrations of bivalence cations and carbonate are totally out of equilibrium with carbonate minerals. In the short term, i.e., the first 10 years, the transport (dispersion and mixing) and dynamic equilibrium determine the evolution of Ca, Mg, and HCO_3^-. The fast dispersion of solutes leads to an increase in Ca and Mg (Figure 21 b), which triggers the dissolution of calcite and precipitation of dolomite (Figure 22), with the reaction as follows:

$$\text{Calcite} + HCO_3^- + Mg^{+2} = H^+ + \text{dolomite} \quad (10)$$

As this reaction keep moving to the right-hand side, HCO_3^- concentration is dragged down (Figure 21b). Mg concentration increases due to the transport process cannot be overcome at the very beginning (less than one year) by the precipitation of dolomite, but Mg starts to go down after 1 year. At around 10 years, as Mg concentration is low enough, reaction (10) reverses and moves toward the left-hand direction, i.e., dolomite dissolves and calcite precipitates, which continues until 1500 years. As a result, the HCO_3^- concentration stays at a relatively high level for this time period. But Mg concentration is disrupted by the precipitation of chlorite and maintained at a relatively low level. At around 1500 years, a turning point is reached — the dolomite precipitation stops, which leads to a sharp drop in Mg concentration.

The evolution of the Fe concentration at point A (Figure 21a, b) is mainly the consequence of two competitive processes: (1) dispersion and mixing, which tends to raise the Fe concentration, and (2) the precipitation of chlorite, which tends to decrease Fe concentration. The competition between these two processes varies over time. Initially (in less than 1 year), the precipitation of chlorite wins the competition, and Fe concentration decreases (Figure 21 b). Later, however, the influent of water with high Fe content raises the Fe concentration at point A and eventually reaches a level very similar to the Fe concentration in the pore water of the clay formation. Around 1500 years, a sharp increase in Fe concentration occurs (Figure 21a, b) due to a significant slowdown in chlorite precipitation. After that, the concentration of Fe remains stable until 10,000 years (Figure 21a, b). Note that canister corrosion is not considered in the model. If this process is included, the behavior of Fe would be different.

Cation exchange reactions interact with other types of reactions, and the changes in exchangeable cations could affect the swelling properties of EBS buffer and probably the migration of radionuclides. Figures 23a and b show the time evolution of four major exchangeable cations from the montmorillonite sites. Although illite forms due to illitization and provides some additional exchange capability, exchangeable sites from illite make a very minimal contribution, because the amount of illite that forms is rather small, a volume fraction of about 0.4% after 10,000 years (Figure 20), and illite also has lower exchangeable capacity. In line with the changes in aqueous concentration of Na, K (Figure 19), Ca, and Mg (Figure 21), exchangeable cations undergo a similar time evolution. As aqueous concentration of Na increases, exchangeable Na increases as well, and eventually becomes the dominant exchangeable cations. Exchangeable Ca initially occupies most exchangeable sites, but starts to decrease after about 10 years, mainly because the precipitation of calcite takes the aqueous Ca, so that Ca is released from exchangeable sites to replenish. The exchangeable sites occupied by Mg also have some fluctuations following the change in aqueous Mg, for the reasons discussed above, but at later stages, decrease in exchangeable Mg is dominant, acting to replenish the aqueous Mg consumed by the precipitation of chlorite (Figure 20). K is also released from the exchangeable sites, mostly to meet the need of K for illitization. Eventually, this K is reduced to a very low level (Figure 23).

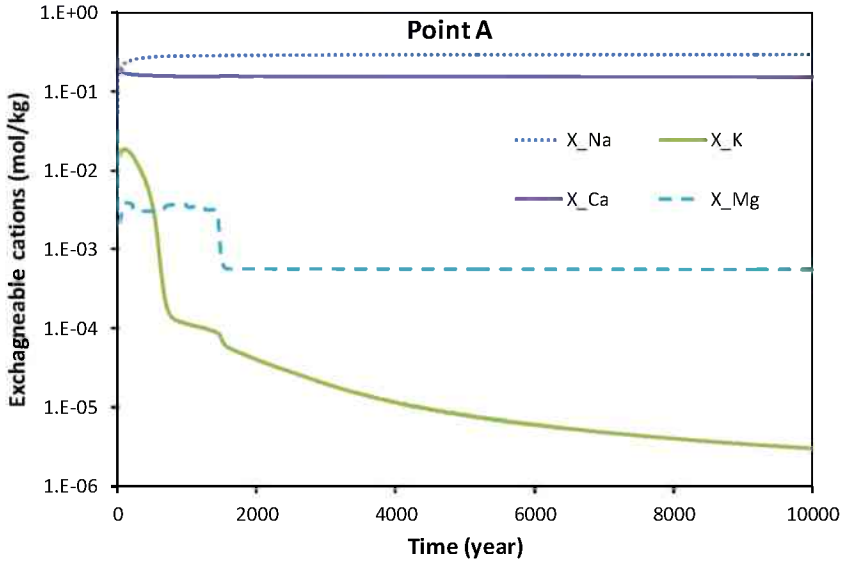

(a)

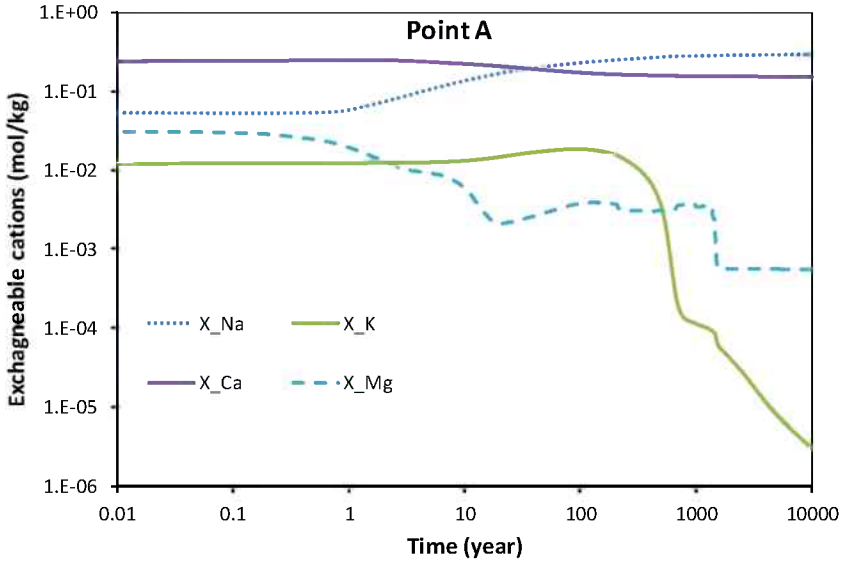

(b)

Figure 23. Time evolution of exchangeable cations at point A with linear (a) and logarithmic (b) time scale.

Protons are involved in many reactions, with the most important ones being the dissolution/precipitation of minerals like montmorillonite, chlorite, illite, dolomite and calcite—and the protonation reaction with surface sorption sites and exchangeable sites. Figures 24 a and b, show the evolution of pH and some important surface protonation species. Around 10 years, when the temperature peaks, montmorillonite dissolves and chlorite precipitates rapidly, which leads to significant drops in pH. As a result, more surface sites are protonated, which is demonstrated by an increase in the concentration of mon-w1OH_2^+ (the protonated species of the weak site type 1 on montmorillonite surface) and ill-w1OH_2^+ (the protonated species of the weak site type 1 on the illite surface) and a corresponding decrease in depronated species mon-w1O^- and il-w1O^-. The rest of the surface proton species is also similarly affected, but their concentrations are orders of magnitude lower and not shown in Figure 24. Also shown in Figure 24 are the protons that go to the exchangeable sites; they show a trend similar to the surface protonated species, but the concentration is much lower.

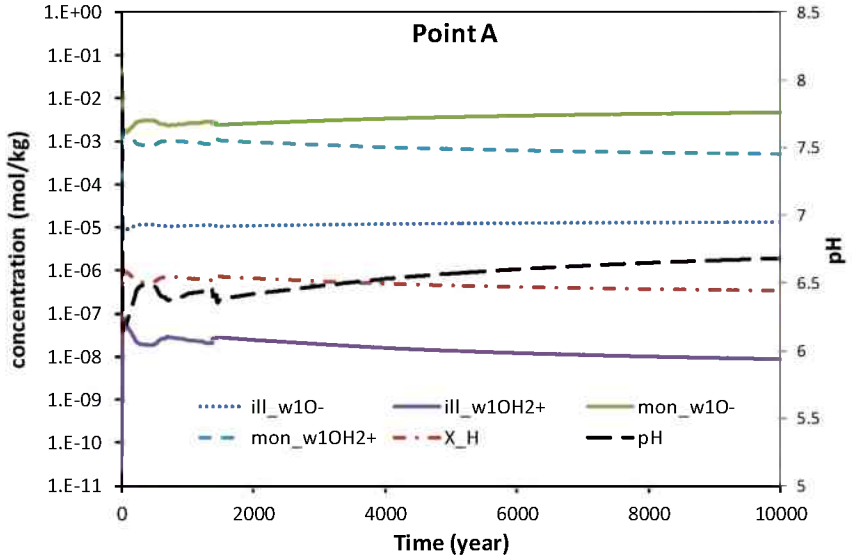

(a)

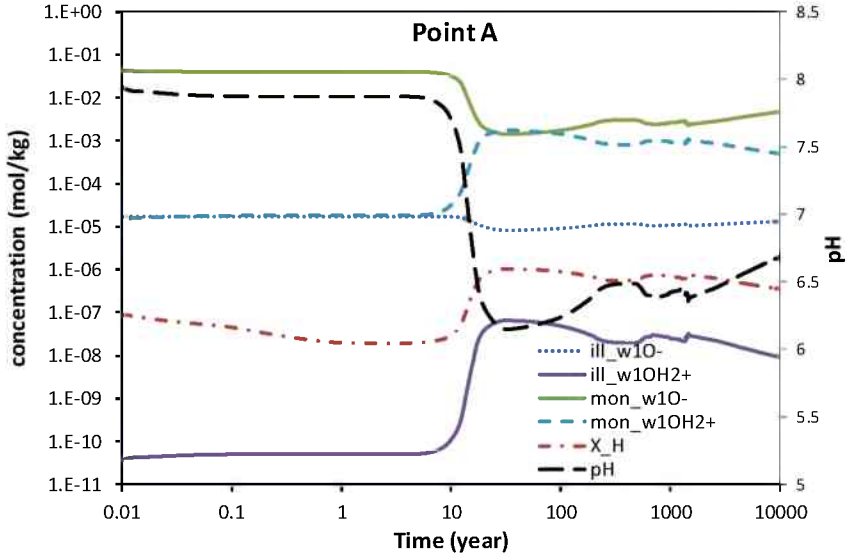

(b)

Figure 24. Time evolution of pH (the right Y axis) and surface protonation species (left Y axis) at point A with linear (a) and logarithmic (b) time scale.

Point B is located in the EBS bentonite adjacent to the bentonite-clay formation interface. The chemical evolution at point B is very similar to that at point A, except at an early stage. The faster hydration at point B leads to a quicker rise in concentrations for all species, for example, Cl, K, and Ca, as shown in Figure 25. After 10 years, the concentration profiles at points A and B almost overlap, although slight differences are observed for K, because K is controlled by illitization, which is affected by temperature, and temperatures at point A and B are different.

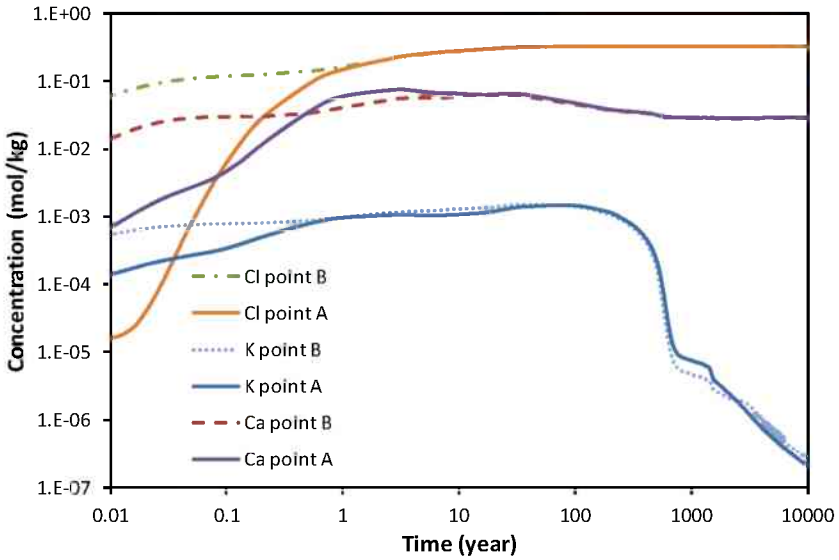

Figure 25. Time evolution of Cl, K, and Ca at point A and B.

Point C is located in the clay formation, close to the bentonite/clay formation interface. Initially, the concentration of Cl decreases, and then recovers (Figure 26 a, b), which represents the effect of dispersion into bentonite and water inflow from the far field of the clay formation. Na behaves similarly to Cl (Figure 26 a, b), although it is affected by chemical reactions. Al concentration drops in the first year (Figure 26 a, b) due to the precipitation of chlorite. Since the Al concentration is very low, very little chlorite precipitation is enough to change the Al concentration significantly. Note that the changes in chlorite in the first year are too small to be seen in Figure 27 a and b. After that, Al concentrations gradually recover as montmorillonite starts to dissolve. Around 670 years, there is a significant change in the chemical system. Before that, K concentration decreased steadily due to the precipitation of illite; SiO_2(aq) concentrations increased steadily due to the dissolution of montmorillonite and chlorite, despite the precipitation of quartz and illite consuming some SiO2(aq). The turning point at 670 years is triggered by the completion of the transformation from calcite and siderite to ankerite (Figure 29). As the ankerite stops precipitating, chlorite dissolution loses its driving force, and chlorite starts to precipitates, which significantly hinders the precipitation of illite. As a result, the decrease in K concentrations becomes very slow. At 1500 years, chlorite precipitation stops; consequently, illite precipitation accelerates and K concentrations undergo a sharp drop. After 1500 years, the K concentration slowly decreases as the dissolution of montmorillonite and the precipitation of illite continue

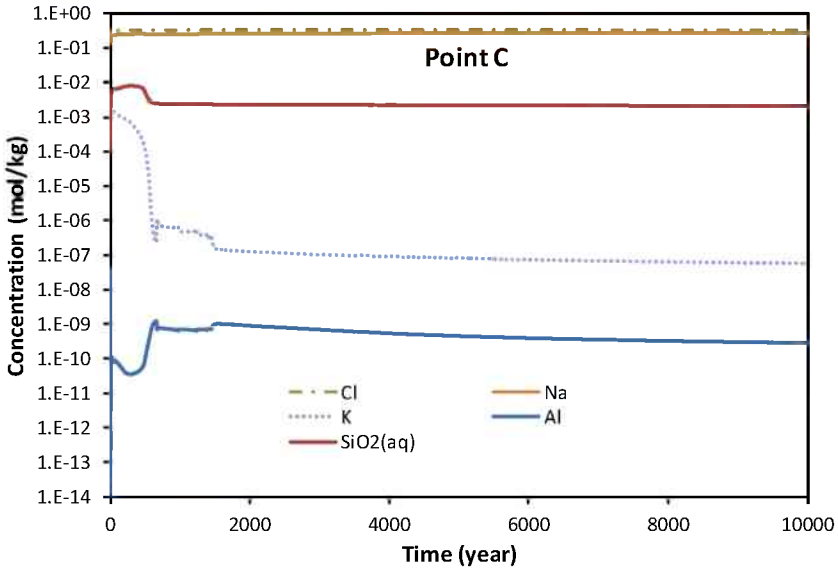

(a)

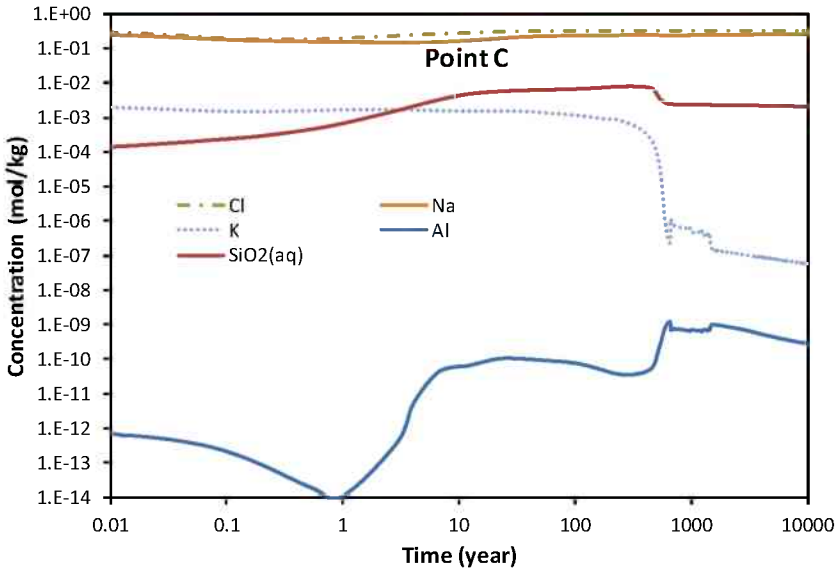

(b)

Figure 26. Time evolution of Cl, Na, and K, Al and SiO_2(aq) concentrations at point C with linear (a) and logarithmic (b) time scale.

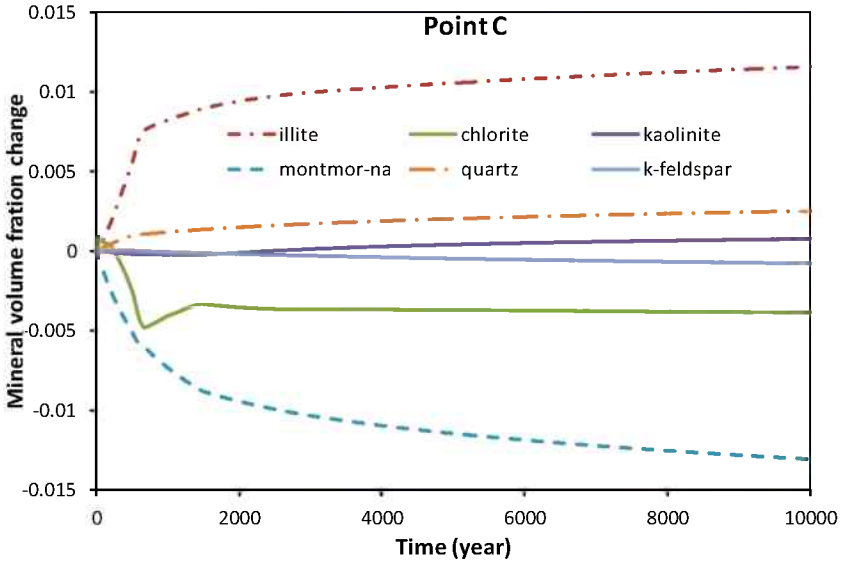

(a)

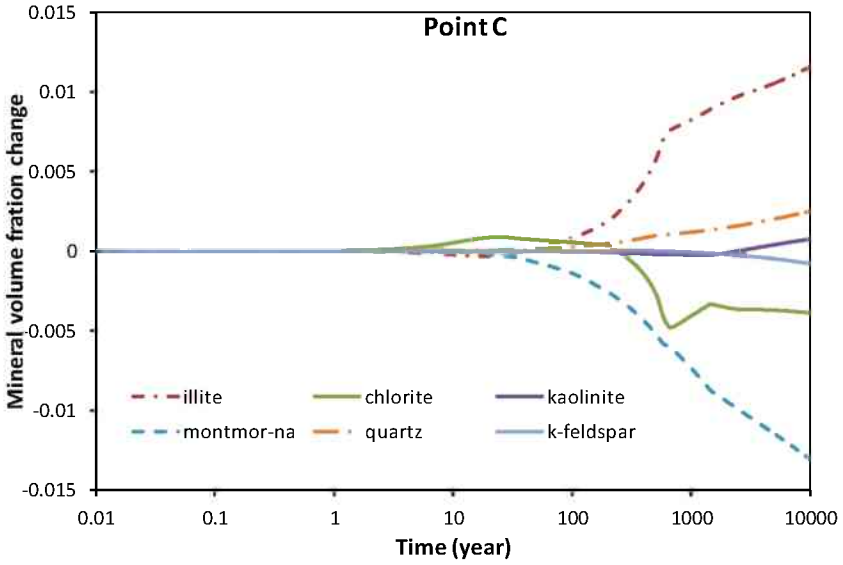

(b)

Figure 27. Time evolution of Al-Si concentrations at point C with linear (a) and logarithmic (b) time scale.

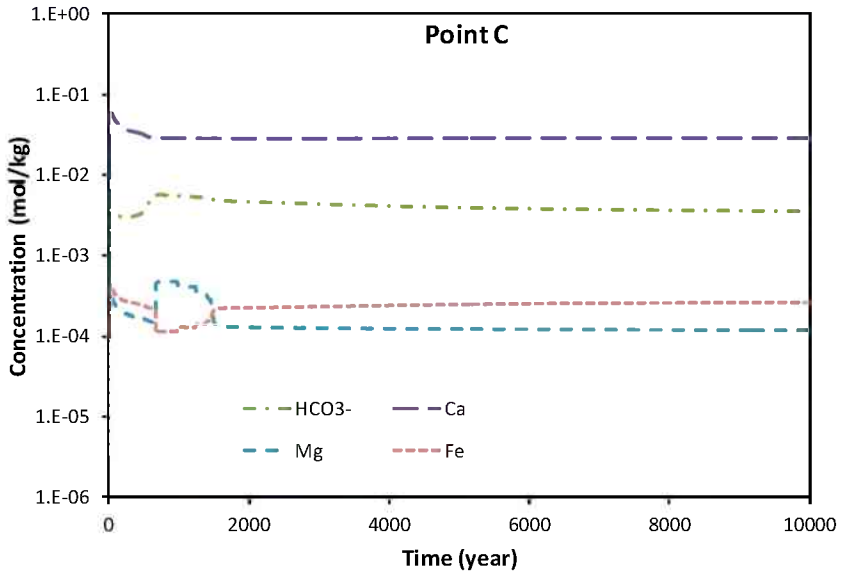

(a)

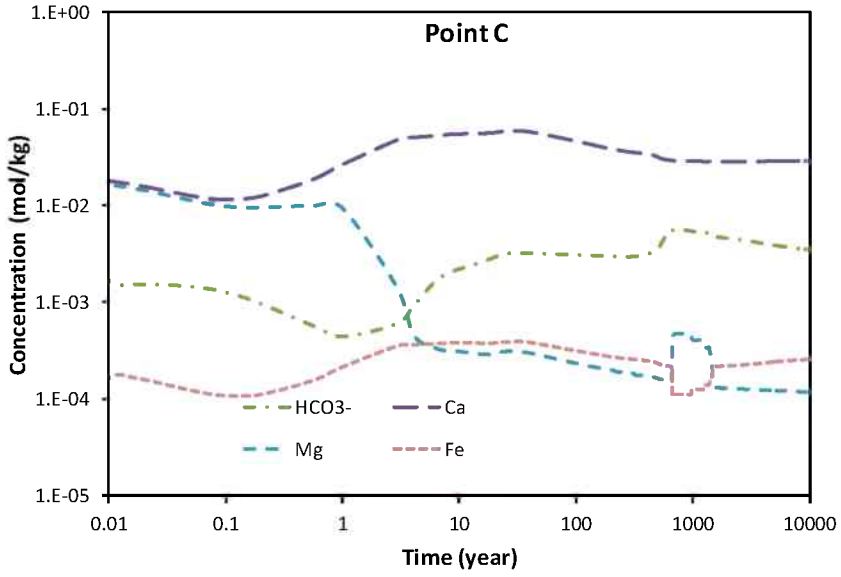

(b)

Figure 28. Time evolution of Ca, Mg, Fe and HCO_3^- concentrations at point C with linear (a) and logarithmic (b) time scale.

At an early stage (less than a couple years), bivalence cations undergo some changes (Figure 28 a, b) to accommodate the hydrodynamic and chemical interactions between EBS bentonite and the clay formation. After that, the transformation of calcite and siderite to ankerite (Figure 29 a, b) leads to an increase in bicarbonate and a decrease in Fe and Mg. But after 670 years, such transformation stops, triggering a series of sudden changes in K, Al, and some Al-Si minerals, as described above.

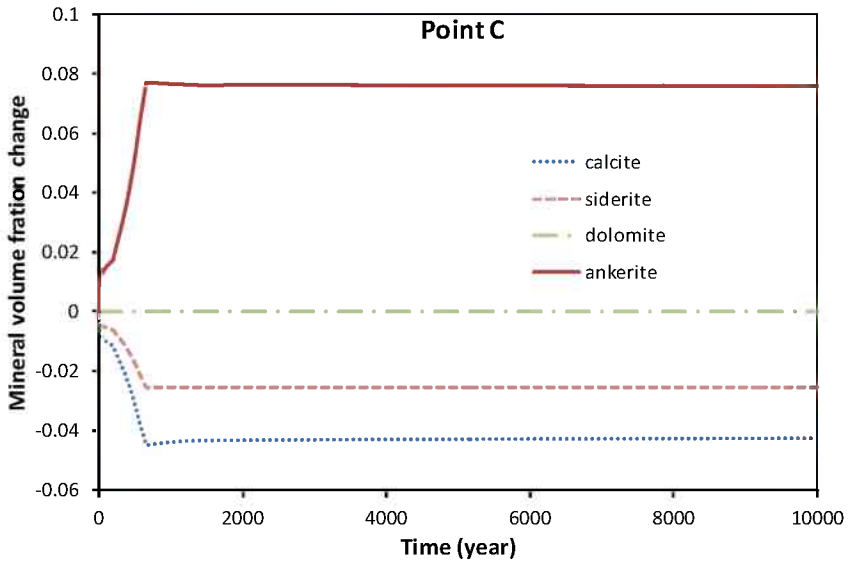

(a)

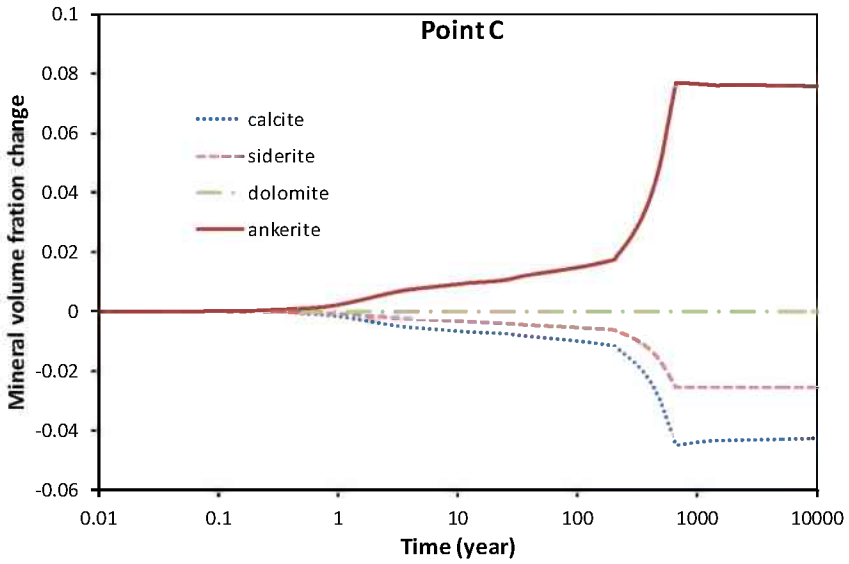

(b)

Figure 29. Time evolution of carbonate minerals at point C with linear (a) and logarithmic (b) time scale.

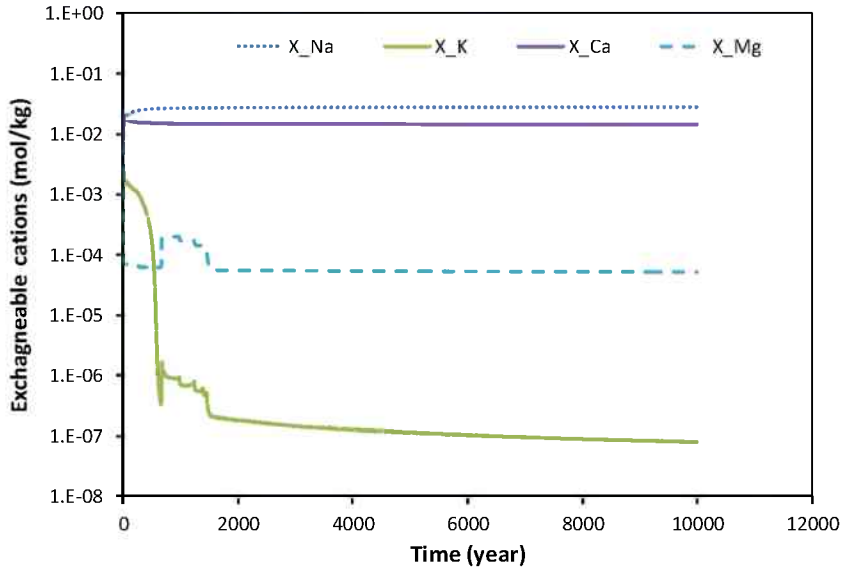

(a)

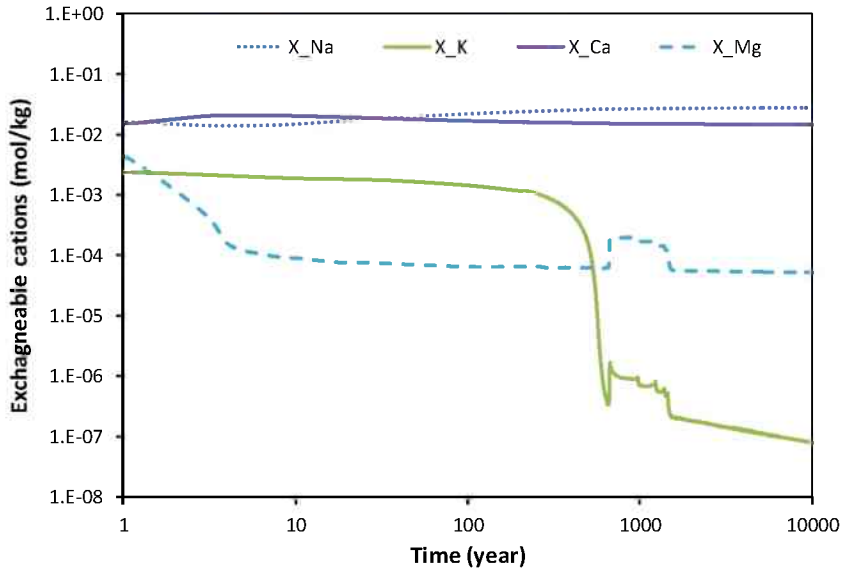

(b)

Figure 30. Time evolution of exchangeable cations at point C with linear (a) and logarithmic (b) time scale.

Exchangeable cations closely follow the changes in their aqueous counterparts. Initially, most sites are occupied by Ca, but later, sites occupied by Na exceed the Ca sites (Figure 30 a, b), which causes a decrease in the weighted average of exchangeable cations. According to Zheng et al. (2011), such changes may lead to a decrease in the swelling capability of the clay formation.

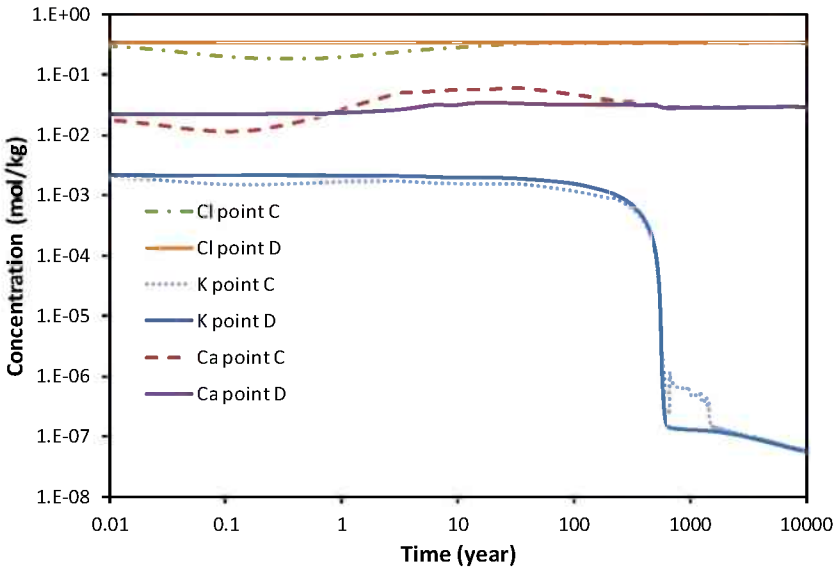

Figure 31. Time evolution of Cl, K and Ca at point C and D.

Point D is located in the clay formation about 10 m away from the bentonite-clay formation interface. As shown by the concentration of Cl (Figure 31a, b), the chemical system is not affected by hydrodynamic processes. But it is known that such formations usually undergo diagenesis processes. One of these processes is illitization, which eventually uses most of the available K in the groundwater, with K concentration becoming very low (Figure 31 a, b).

3.2.2 U(VI) migration

In our current model, it is assumed that canisters have collapsed after 1000 years. Figure 32 shows the concentration of U(VI) at the canister assumed to be composed of pure schoepite. The concentration of U(VI) is mainly controlled by the dissolution of schoepite, but also affected by the concentration of calcium and carbonate, since the Ca-U-carbonate aqueous complexes is the dominant U(VI) aqueous species. A maximum concentration of about 1 mM could be reached.

U(VI) leaches out of the canister and move into the EBS bentonite by diffusion and dispersion. Concentrations of U(VI) at point A, the closest point in the bentonite adjacent to the canister, increase quickly, and the temporal delay is hardly noticeable. However, bentonite possesses very strong sorption capability and adsorbs most of the U(VI). As shown in Figure 33, the concentration of sorbed U(VI) increases significantly. As a result, the concentration of aqueous U(VI) increases only to about 1e-4 M, about one order of magnitude lower than that at the canister. Cation exchange does not contribute substantially enough to retard the migration of U(VI) in current simulations. Figure 33 shows the U(VI) on exchangeable sites ($X\_UO_2^{+2}$) is about 6 orders of magnitude lower than that at sorption sites.

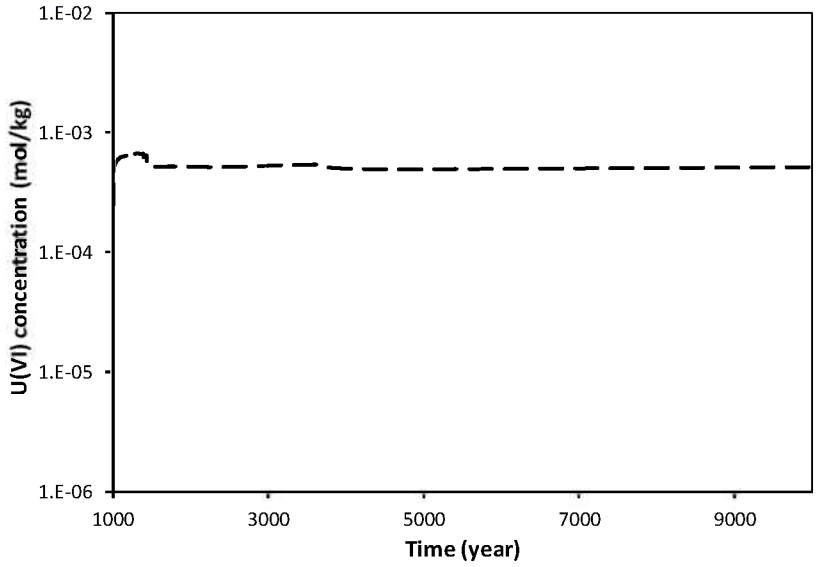

Figure 32. Time evolution of total U(VI) concentration at canister.

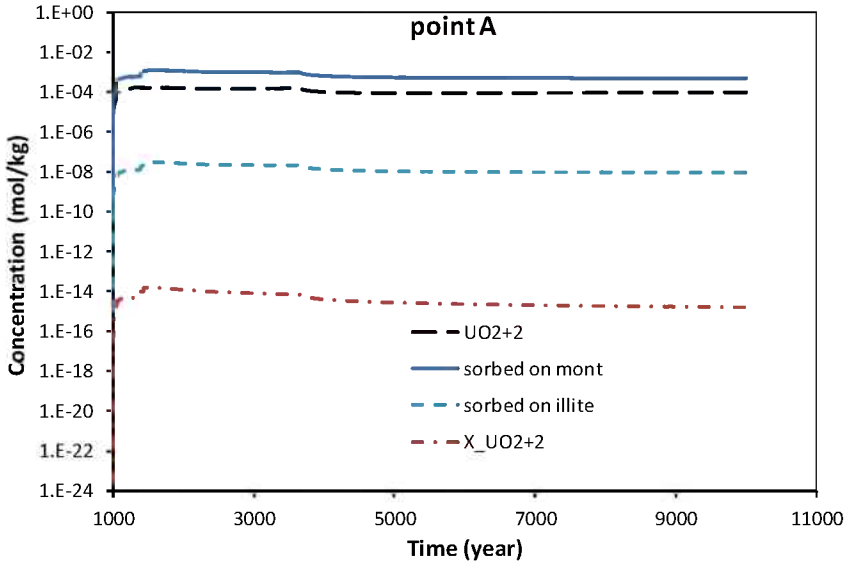

Figure 33. Time evolution of U(VI) concentration on sorption sites (sorbed UO_2^{+2}), exchangeable sites ($X\_UO_2^{+2}$) and aqueous phase at point A.

Figure 34 shows the temporal breakthrough of U(VI) at six monitoring locations. Point A is near the canister and Point B is close to the bentonite-host rock interface, but located in the bentonite. Point C is the first node in the host clay formation beyond the bentonite-host rock interface. Points D, E, and F are well inside the clay formation, at distances to the bentonite-host rock interface of about 10, 20 and 450 m, respectively. Model results show that U(VI) quickly breaks through the EBS bentonite. It takes about 100 years for U(VI) to appear at Point D and then about 200 years to reach Point E. Slight increases in U(VI) concentration are also observed at Point E 500 years after the release of U(VI) from the canister. But the concentration remains very low after 10,000 years.

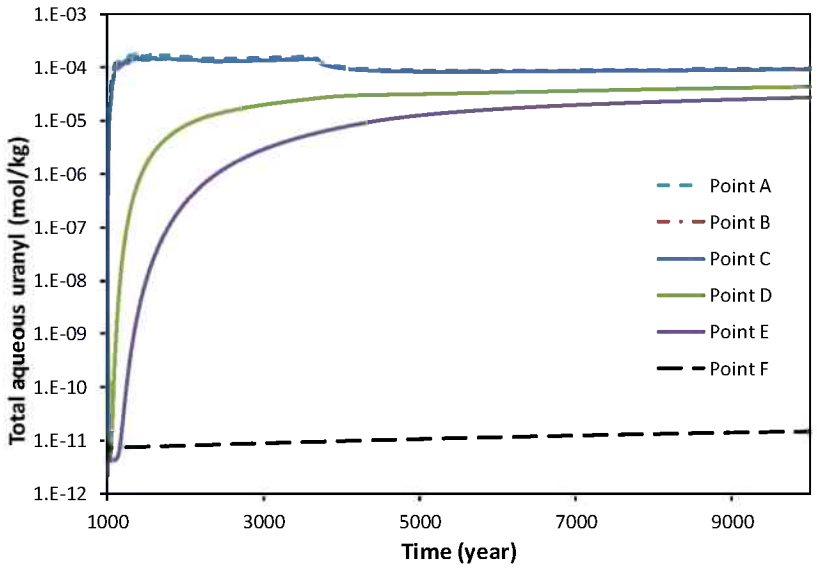

Figure 34. Time evolution of aqueous U(VI) concentration at point A, B, C, D, E, and F.

Figures 35 and 36 show the spatial distribution of aqueous U(VI) concentration at 1000 and 10,000 years, respectively. Symmetry is observed in both X and Z directions, indicating the model domain could be one quarter of the current domain, which would save substantial computation time.

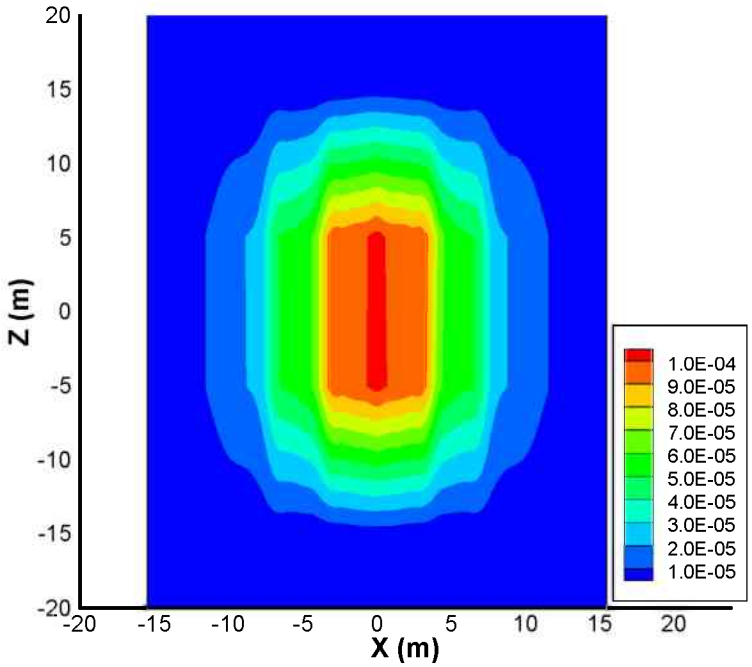

Figure 35. Spatial distribution of aqueous U(VI) concentration at 1000 years.

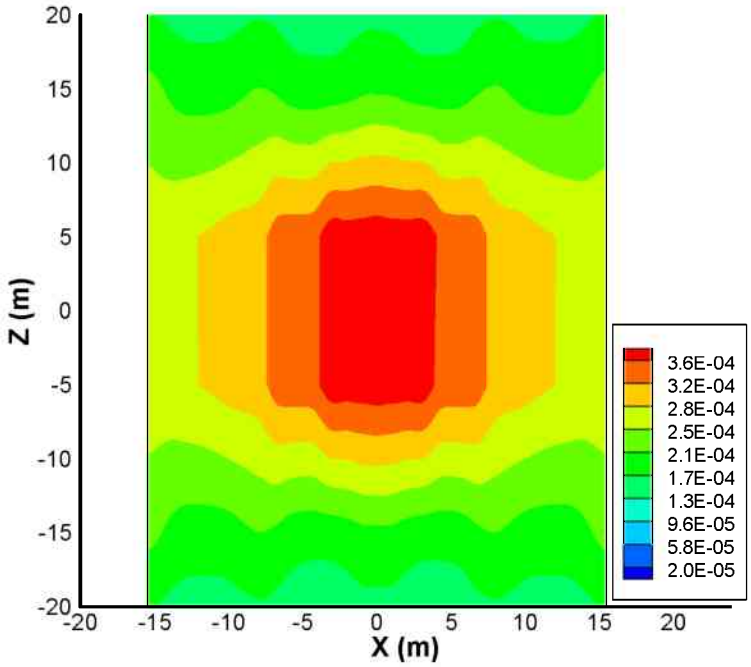

Figure 36. Spatial distribution of aqueous U(VI) concentration at 10,000 years.

Figure 37 shows temporal profiles of sorbed U(VI) concentration at points A, B, C, D, E, and F. Sorbed U(VI) concentration is the sum of each individual surface species listed in Table 2. The current model considers the adsorption of U(VI) on illite and smectite. In EBS bentonite, smectite is initially the only adsorbent. As illitization continues, illite forms and adsorbs U(VI) as well, but with a rather minimal contribution to total sorbed U(VI) in EBS. In the host clay formation, both illite and smectite can adsorb U(VI). At points B and C, although the aqueous U(VI) concentrations are very similar (see Figure 27), the total sorbed U(VI) concentrations are quite different.

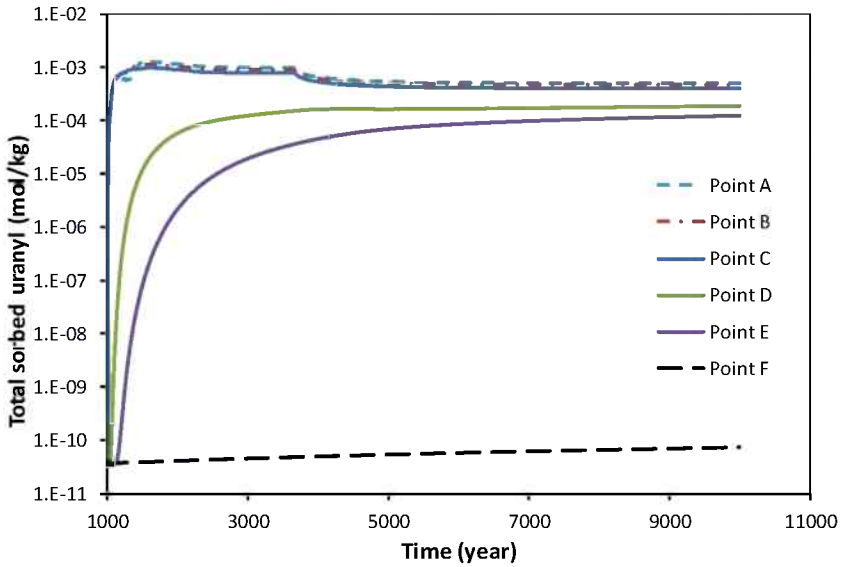

Figure 37. Time evolution of aqueous U(VI) concentration at points A, B, C, D, E, and F.

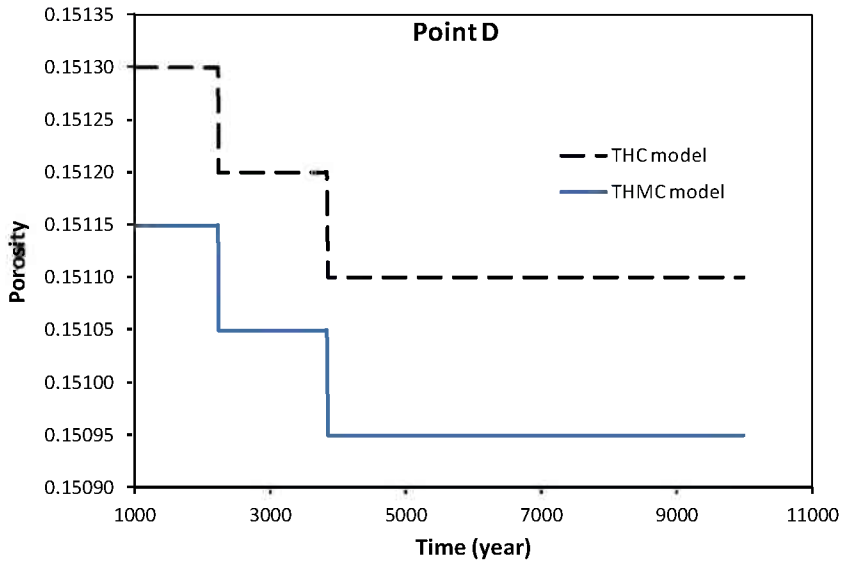

Figure 38. Time evolution of porosity obtained with THC and THMC models.

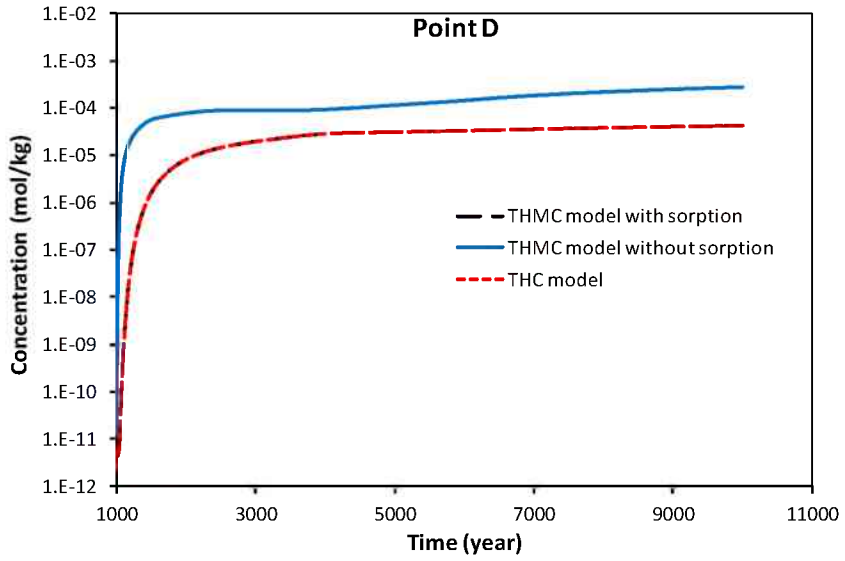

Figure 39. A comparison of the time evolution of aqueous U(VI) concentration at Point D in several scenarios.

Since the EDZ is not considered yet in this study and diffusion is the dominant transport process for U(VI) migration, mechanical changes affect the migration of U(VI) rather indirectly —swelling changes porosity and subsequently the tortuosity via the model of Millington and Quirk (1961) (see Table 6 for the relation between porosity and tortuosity). Both mineral precipitation/dissolution and stress changes can change the porosity. However, as shown in Figure 38, in clay formations the porosity changes due to mineral precipitation/dissolution overshadows the porosity changes by mechanical reason. Note that the discontinuity of curves is caused by the truncation of numbers. Therefore, the THC model, which does not consider mechanical processes, shows a U(VI) migration very similar to the THMC model; for example, the breakthrough curve at Point D as shown in Figure 39. Also shown in Figure 39 is a model

that does not consider sorption (or surface complexation) reactions. Consideration of sorption makes significant difference in model results.

4. CONCLUSIONS AND FUTURE WORK

For clay formations, coupled thermal, hydrological, mechanical, and chemical (THMC) processes are expected to have a significant impact on the long-term safety of a clay repository. These coupled processes may affect radionuclide transport specifically by changing transport paths (e.g., formation and evolution of EDZ) and altering flow, mineral, and mechanical properties that are related to radionuclide transport. The objectives of this research activity are to improve the modeling capability for coupled THMC processes and to use that improved capability to evaluate the THMC impacts on radionuclide transport. Our FY12 accomplishments include:

- The TOUGHREACT-FLAC3D simulator developed in Zheng et al. (2011) was further enhanced by incorporation of the 2 site protolysis non-electrostatic surface complexation and cation exchange sorption model (2 SPNE SC/CE) (Bradbury and Baeyens, 2011) for U(VI).
- Coupled THMC simulations have been conducted to demonstrate the usefulness of the TOUGHREACT-FLAC3D simulator and to evaluate the THMC impacts on U(VI) transport.

The major findings from the THMC simulations include

- The chemical-mechanical coupling based on linear elastic swelling model leads to 5% difference in effective stress compared with the model that ignores such coupling effect before the EBS bentonite becomes fully saturated.
- Ca and bicarbonate concentrations have a significant effect on U(VI) transport by aqueous complexation. A reactive transport model that neglects such an effect may underestimate the U(VI) concentration and migration rate.
- Montmorillonite is the most important adsorbent for U(VI) in clay formations, although its content in these formations is less than that of illite. Surface complexation plays a major role in adsorbing U(VI), whereas cation exchange does not make a significant contribution toward retarding the migration of U(VI).
- The effect of mechanical processes on the migration of U(VI) seems not be significant for an undamaged clay repository according to the current modeling results.

For the remaining months of FY12, we will

- Perform sensitivity analyses by varying major THMC parameters to further evaluate the impact of coupled THMC processes on the migration of U(VI) in clay formations.

For FY13, we propose the following tasks

- Refine the chemical model (such as including redox reactions). In the current model, it is assumed that the system is under oxidizing conditions and that such conditions persist for 10,000 years. Changes in redox conditions may significantly change the behavior of uranium.
- Include EDZ in the current model.
- Develop and test other chemical-mechanical coupling constitutive relationships.

ACKNOWLEDGMENTS

Funding for this work was provided by the Used Fuel Disposition Campaign, Office of Nuclear Energy, of the U.S. Department of Energy under Contract Number DE-AC02-05CH11231 with Lawrence Berkeley National Laboratory.

5. REFERENCES

Appelo, C. J. A. and D. Postma, *Geochemistry, groundwater and pollution*. Rotterdam, Netherlands, A.A.Balkema (1994).

Appelo, C. A. J., L. R. Van Loon and P. Wersin, Multicomponent diffusion of a suite of tracers (HTO, Cl, Br, I, Na, Sr, Cs) in a single sample of Opalinus Clay. *Geochimica et Cosmochimica Acta* 74(4): 1201-1219 (2010).

Arai, Y., M. McBeath, J. R. Bargar, J. Joye and J. A. Davis, Uranyl adsorption and surface speciation at the imogolite–water interface: Self-consistent spectroscopic and surface complexation models. *Geochimica et Cosmochimica Acta* 70(10): 2492-2509 (2006).

Arda, D., J. Hizal and R. Apak, Surface complexation modelling of uranyl adsorption onto kaolinite based clay minerals using FITEQL 3.2. *Radiochimica Acta* 94(12): 835-844 (2006).

Barnichon J.D. and G. Volckaert, Observations and Predictions of Hydromechanical Coupling Effects in the Boom Clay, Mol Underground Research Laboratory, Belgium, *Hydrogeology Journal* 11 (1), 193-202 (2003).

Bernot, P., Dissolved concentration limits of radioactive elements, ANL-WIS-MD-000010 REV 05 (2005).

Bernhard, G., G. Geipel, T. Reich, V. Brendler, S. Amayri and H. Nitsche, Uranyl(VI) carbonate complex formation: Validation of the Ca2UO2(CO3)3(aq.) species. *Radiochimica Acta* 89(8_2001): 511 (2001).

Bethke C. M. and P. V. Brady, How the Kd Approach Undermines Group Water Cleanup. *Ground Water* 38, 435–443 (2000).

Bradbury, M. H. and B. Baeyens, Modelling the sorption of Mn(II), Co(II), Ni(II), Zn(II), Cd(II), Eu(III), Am(III), Sn(IV), Th(IV), Np(V) and U(VI) on montmorillonite: Linear free energy relationships and estimates of surface binding constants for some selected heavy metals and actinides. *Geochimica et Cosmochimica Acta* 69(4): 875-892 (2005).

Bradbury, M. H. and B. Baeyens, Sorption modelling on illite Part I: Titration measurements and the sorption of Ni, Co, Eu and Sn. *Geochimica et Cosmochimica Acta* 73(4): 990-1003 (2009a).

Bradbury, M. H. and B. Baeyens, Sorption modelling on illite. Part II: Actinide sorption and linear free energy relationships. *Geochimica et Cosmochimica Acta* 73(4): 1004-1013 (2009b).

Bradbury, M. H. and B. Baeyens, Predictive sorption modelling of Ni(II), Co(II), Eu(IIII), Th(IV) and U(VI) on MX-80 bentonite and Opalinus Clay: A "bottom-up" approach. *Applied Clay Science* 52(1–2): 27-33 (2011).

Catalano, J. G. and G. E. Brown Jr, Uranyl adsorption onto montmorillonite: Evaluation of binding sites and carbonate complexation. *Geochimica et Cosmochimica Acta* 69(12): 2995-3005 (2005).

Davis, J. A., J. A. Coston, D. B. Kent and C. C. Fuller, Application of the Surface Complexation Concept to Complex Mineral Assemblages. *Environmental Science & Technology* 32(19): 2820-2828 (1998).

Davis, J. A., D. E. Meece, M. Kohler and G. P. Curtis, Approaches to surface complexation modeling of Uranium(VI) adsorption on aquifer sediments. *Geochimica et Cosmochimica Acta* 68(18): 3621-3641 (2004).

De Windt, L., A. Burnol, P. Montarnal and J. van der Lee, Intercomparison of reactive transport models applied to UO2 oxidative dissolution and uranium migration. *Journal of Contaminant Hydrology* 61(1–4): 303-312 (2003).

De Windt, L., H. Schneider, C. Ferry, H. Catalette, V. Lagneau, C. Poinssot, A. Poulesquen and C. Jegou, Modeling spent nuclear fuel alteration and radionuclide migration in disposal conditions. *Radiochim. Acta* 94: 787-794 (2006)..

Fernández, A. M., M. J. Turrero, D. M. Sánchez, A. Yllera, A. M. Melón, M. Sánchez, J. Peña, A. Garralón, P. Rivas, P. Bossart and P. Hernán, On site measurements of the redox and carbonate system parameters in the low-permeability Opalinus Clay formation at the Mont Terri Rock Laboratory. *Physics and Chemistry of the Earth*, Parts A/B/C 32(1-7): 181-195 (2007).

Fouche O., Wright H., Cleach J. L., and Pellenard P., Fabric Control on Strain and Rupture of Heterogeneous Shale Samples by Using a Non-Conventional Mechanical Test, *Applied Clay Science* 26, 367-387 (2004).

Garcia-Gutierrez, M., J. L. Cormenzana, T. Missana, M. Mingarro, U. Alonso, J. Samper, Q. Yang and S. Yi, Diffusion experiments in Callovo-Oxfordian clay from the Meuse/Haute-Marne URL, France. Experimental setup and data analyses. *Physics and Chemistry of the Earth* 33: S125-S130 (2008).

Garcia-Gutierrez, M., J. L. Cormenzana, T. Missana, M. Mingarro and P. L. Martin 2006. Large-scale laboratory diffusion experiments in clay rocks. *Physics and Chemistry of the Earth* 31(10-14): 523-530.

Gao, L., Z. Yang, K. Shi, X. Wang, Z. Guo and W. Wu, U(VI) sorption on kaolinite: effects of pH, U(VI) concentration and oxyanions. *Journal of Radioanalytical and Nuclear Chemistry* 284(3): 519-526 (2010).

Gu, X., L. J. Evans and S. J. Barabash, Modeling the adsorption of Cd (II), Cu (II), Ni (II), Pb (II) and Zn (II) onto montmorillonite. *Geochimica et Cosmochimica Acta* 74(20): 5718-5728 (2010).

Korichi, S. and A. Bensmaili 2009. Sorption of uranium (VI) on homoionic sodium smectite experimental study and surface complexation modeling. Journal of Hazardous Materials 169(1-3): 780-793.

Laredj, N., H. Missoum and K. Bendani, Modeling the effect of osmotic poential changes on deformation behavior of swelling clays. *Journal of Porous Media* 13(8): 743-748 (2010).

Lauber, M., Baeyens, B., Bradbury, M.H., Sorption of Cs, Sr, Ni, Eu, Th, Sn and Se on Mont Terri Opalinus Clay: physico-chemical characterisation and sorption measurements. PSI Bericht Nr. 00-10 Paul Scherrer Institut, Villigen, Switzerland and Nagra NTB 00-11, Nagra, Wettingen, Switzerland (2000).

Maes, N., S. Salah, D. Jacques, M. Aertsens, M. Van Gompel, P. De Cannière and N. Velitchkova, Retention of Cs in Boom Clay: Comparison of data from batch sorption tests and diffusion experiments on intact clay cores. *Physics and Chemistry of the Earth*, Parts A/B/C 33(Supplement 1): S149-S155 (2008).

McKinley, J. P., J. M. Zachara, S. C. Smith and G. D. Turner, The influence of uranyl hydrolysis and multiple site-binding reactions on adsorption of U(VI) to montmorillonite. *Clays and Clay Minerals* 43(5): 586-598 (1995).

Müller-Vonmoos, M., Kahr, G., Mineralogische untersuchungen von wyoming bentonite MX-80 und montigel. NTB 83-13, Nagra, Wettingen, Switzerland (1983).

Ochs, M., B. Lothenbach, M. Shibata and M. Yui. Thermodynamic modeling and sensitivity analysis of porewater chemistry in compacted bentonite. *Physics and Chemistry of the Earth*, Parts A/B/C 29(1): 129-136 (2004).

Patriarche D., Ledoux E., Simon-Coincon R., Michelot J., and Cabrera J, Characterization and Modeling of Diffusive Process for Mass Transport through the Tournemire Argillites Aveyron, France, *Applied Clay Science* 26: 109-122 (2004).

Pruess, K., C. Oldenburg and G. Moridis, TOUGH2 User's Guide, Version 2.0, Lawrence Berkeley National Laboratory, Berkeley, CA (1999).

Pruess, K., The TOUGH Codes— a family of simulation tools for multiphase flow and transport processes in permeable media. *Vadose Zone Journal*, 3: 738–746 (2004).

Rutqvist, J., Barr, D., Birkholzer, J.T., Fujisaki, K., Kolditz, O., Liu, Q.-S., Fujita, T., Wang, W., Zhang, C.-Y., A comparative simulation study of coupled THM processes and their effect on fractured rock permeability around nuclear waste repositories. *Environmental Geology* 57, 1347–1360 (2009).

Rutqvist, J., Status of the TOUGH-FLAC simulator and recent applications related to coupled fluid flow and crustal deformations. *Computers & Geosciences* 37(6): 739-750 (2011).

Sonnenthal, E., A. Ito, N. Spycher, M. Yui, J. Apps, Y. Sugita, M. Conrad and S. Kawakami, Approaches to modeling coupled thermal, hydrological, and chemical processes in the Drift Scale Heater Test at Yucca Mountain. *Int. J. Rock Mech. Min. Sci.* 42: 6987–6719 (2005).

Sonnenthal, E. Chapter 5 in: Birkholzer, J. Rutqvist, E. Sonnenthal, and D. Barr, Long-Term Permeability/Porosity Changes in the EDZ and Near Field due to THM and THC Processes in Volcanic and Crystalline-Bentonite Systems, DECOVALEX-THMC Project Task D Final Report, 2008.

Soler, J. M., J. Samper, A. Yllera, A. Hernández, A. Quejido, M. Fernández, C. Yang, A. Naves, P. Hernán and P. Wersin, The DI-B in situ diffusion experiment at Mont Terri: Results and modeling. *Physics and Chemistry of the Earth*, Parts A/B/C 33(Supplement 1): S196-S207 (2008).

Spycher, N., K. Pruess and J. Ennis-King, CO_2-H_2O mixtures in the geological sequestration of CO_2. I. Assessment and calculation of mutual solubilities from 12 to 100°C and up to 600 bar. *Geochimica et Cosmochimica Acta*, 67(16): 3015-3031 (2003).

Spycher, N. F., M. Issarangkun, B. D. Stewart, S. Sevinç Şengör, E. Belding, T. R. Ginn, B. M. Peyton and R. K. Sani, Biogenic uraninite precipitation and its reoxidation by iron(III) (hydr)oxides: A reaction modeling approach. *Geochimica et Cosmochimica Acta* 75(16): 4426-4440 (2011).

Tang C. A. and Hudson J.A. *Rock Failure Mechanisms*, Taylor & Francis, London, UK (2010).

Tournassat, C., E. Ferrage, C. Poinsignon and L. Charlet, The titration of clay minerals: II. Structure-based model and implications for clay reactivity. *Journal of Colloid and Interface Science* 273(1): 234-246 (2004).

Thury, M., The characteristics of the Opalinus Clay investigated in the Mont Terri underground rock laboratory in Switzerland. *Comptes Rendus Physique* 3(7-8): 923-933 (2002).

Van Loon, L. R., P. Wersin, J. M. Soler, J. Eikenberg, T. Gimmi, P. Hernan, S. Dewonck and S. Savoye, In-situ diffusion of HTO, $^{22}Na^{+}$, Cs^{+} and I^{-} in Opalinus clay at the Mont Terri underground rock laboratory. *Radiochim. Acta* 92: 757-763 (2004).

Wronkiewicz, D.J.; Bates, J.K.; Wolf, S.F.; and Buck, E.C. Ten-year results from unsaturated drip tests with UO_2 at 90°C: implications for the corrosion of spent nuclear fuel. *Journal of Nuclear Materials, 238,* (1), 78-95 (1996).

Wu, T., S. Amayri, J. Drebert, L. R. Van Loon and T. Reich, Neptunium(V) Sorption and Diffusion in Opalinus Clay. Environmental Science & Technology 43(17): 6567-6571 (2009).

Xu, T., N. Spycher, E. Sonnenthal, G. Zhang, L. Zheng and K. Pruess, TOUGHREACT Version 2.0: A simulator for subsurface reactive transport under non-isothermal multiphase flow conditions. Computers & Geosciences 37(6): 763-774 (2011).

Xu, T. and K. Pruess, Modeling multiphase non-isothermal fluid flow and reactive geochemical transport in variably saturated fractured rocks: *1 Methodology. Am. J Sci*. 301: 16–33 (2001).

Xu, T. and K. Pruess. Numerical studies on enhanced CO_2 dissolution and mineral trapping due to formation of aqueous complexes. *Computational Methods in Water Resources*. San Francisco, California (2008).

Xu, T., E. Sonnenthal, N. Spycher and K. Pruess, TOUGHREACT: A simulation program for non-isothermal multiphase reactive geochemical transport in variably saturated geologic media. *Computers and Geosciences* 32: 145-165 (2006).

Zhang G., Spycher N., Sonnenthal E., Steefel C., and Xu T., Modeling reactive multiphase flow and transport of concentrated aqueous solutions. *Nuclear Technology*, 164, 180-195 (2008).

Zheng, L., J. A. Apps, Y. Zhang, T. Xu and J. T. Birkholzer. On mobilization of lead and arsenic in groundwater in response to CO_2 leakage from deep geological storage. *Chemical geology* 268(3-4): 281-297 (2009).

Zheng, L., J. Rutqvist, J. Houseworth, J. Davis, R. Tinnacher, L. Li and H-H Liu, Investigation of near-field THMC coupled processes, milestone report in UFD, Work Package number 1.02.08.03 (2011).